ELSEVIER

Contents lists available at ScienceDirect

Chemical Engineering Journal

journal homepage: www.elsevier.com/locate/cej





Influence of catalyst shape on plasma-assisted dry reforming of methane: A comparative study of Ni-CeO₂ nano-cubes and nano-octahedra

Md Monir Hossain a, Md Robayet Ahasan b, Ruigang Wang a,*

- a Department of Chemical Engineering and Materials Science, Michigan State University, East Lansing, MI 48824, United States
- ^b Department of Metallurgical and Materials Engineering, The University of Alabama, Tuscaloosa, AL 35487, United States

ARTICLE INFO

Keywords:
Catalyst morphology effect
Ni-CeO₂ nanocatalyst
Plasma-assisted DRM
Plasma DRM Reaction Analysis

ABSTRACT

This study investigated the performance of 10 wt% Ni-CeO $_2$ nano-cubes (NC) and nano-octahedra (NO) shaped catalysts in plasma-assisted dry reforming of methane (DRM) environment to understand the influence of catalyst morphology on catalytic activity and global reaction pathway. The presence of different exposed crystal planes (i. e., (111), (110), and (100)) in the CeO $_2$ shapes led to varied NiO $_3$ -CeO $_2$ interactions, with the NO-shaped catalyst exhibiting a higher oxygen vacancy concentration, lattice defects, and moderate basic sites compared to the NC catalyst. This interaction in the plasma DRM environment significantly enhances conversions for both shaped catalysts, with the effect more pronounced in the case of the NO-shaped catalyst. The performance data suggest that running plasma DRM at moderate temperature and higher plasma power is relatively efficient. Increasing temperatures or plasma power diverts the DRM reaction towards more H $_2$ production, reducing CO production for both shaped catalysts. This confirms the crucial role of the catalyst in controlling the global reaction pathway considering plasma power or temperature enhancement. Plasma interactions create additional surface defects during the DRM reaction, and defect concentration is closely linked to catalyst morphology. Carbon deposits on the catalyst surface can be readily removed via CO $_2$ plasma regeneration treatment without affecting catalyst performance. Additionally, prolonged plasma exposure leads to NiO phase separation into concentrated Ni, suggesting a cyclical DRM and regeneration approach rather than a continuous reaction.

1. Introduction

The increase in energy demand with economic growth is driving more combustion of fossil fuels, even in recent years, where 78 % of energy demand is met by fossil fuels [1]. One primary concern is the high CO₂ emissions (38,522 Mton in 2022) from burning fossil fuels, accounting for 71.6 % of the total greenhouse emission (53,786.04 Mton CO₂-eq in 2022). Another significant greenhouse gas (GHG), CH₄, which comes from fossil fuels and agricultural processes, has an impact 27-30 times greater than CO2, contributing 21 % to total greenhouse gas emissions [2]. The promising dry reforming of methane (DRM) most suitably utilizes these two GHGs and produces syngas (a mixture of H₂ and CO) with a lower H₂/CO ratio, which can be used in several chemical productions, including synthetic oil via the Fischer-Tropsch process [3], and can also be used in power generation. The endothermic nature of DRM reaction limits its viability on a commercial scale due to high temperature (more than 1000 °C), where below 650 °C, the reaction is non-spontaneous. The thermal catalytic path retards temperature down to 600 - 900 °C to get reasonable performance using different catalysts, including noble metals (such as Ru, Pt, Rh) and transition metals (Co, Ni, Mg, Ag) or metal oxides [4–6]. Despite its resistance to coke formation, the noble metal is not deemed suitable for industrial applications due to its elevated cost. Among non-noble metals, nickel (Ni) is particularly renowned for its high catalytic activity in DRM despite its susceptibility to coking and sintering, which can lead to rapid catalyst deactivation.

The efficacy of DRM is intricately tied to catalyst design and surface engineering, which profoundly influence reaction kinetics [7,8]. Incorporating non-thermal plasma, particularly dielectric barrier discharge (DBD), is a promising technique for enhancing catalysis in DRM reactions. DBD plasma modifies catalyst surface properties by introducing reactive species, including ions, radicals, and excited species [9]. Integrating surface-engineered catalysts with DBD plasma may have the potential to enhance reaction kinetics by combining the advantages of both, particularly in improving low-temperature DRM reactions. Researchers have extensively investigated surface-engineered catalysts for

E-mail address: rwang@msu.edu (R. Wang).

^{*} Corresponding author.

thermal DRM and demonstrated their reliability in influencing reaction kinetics. For instance, Li et al. [10] thoroughly investigated Ni/La₂O₃ nanorods catalysts for thermal DRM. The nanorod-shaped La₂O₃ support facilitated the dispersion of Ni particles, exposing active sites and ensuring stability over a 50 h reaction period. Additionally, the nanorodshaped La₂O₃ support enhanced the presence of medium-strength basic sites, promoting improved CO2 adsorption. Consequently, the optimized catalyst configuration substantially enhanced CH₄ (70 %) and CO₂ (75 %) conversions at 700 °C. Gonzalez et al. [11] observed similar highly dispersive behavior of Ni clusters when supported on \gamma-Al2O3 nanofibers. The nanofiber morphology contributed to the catalyst's stability, enabling continuous operation for 55 h at 750 $^{\circ}$ C. Another study by Shen et al. [12] investigated the impact of Al2O3 support morphology on catalytic performance, employing nanosheets (S), nanofibers (F), and particles (P). The Ni/Al₂O₃-S catalyst exhibited high catalytic activity due to effective Ni anchoring on the (110) plane of Al₂O₃-S. Tan et al. [13] investigated ZrO₂-supported Ni catalysts with rod and mixed shapes. These configurations promoted a strong metal-support interaction (SMSI), limiting the cleavage of C-H bonds due to the presence of multiple facets.

On the other hand, DBD plasma can play a crucial role in activating adsorbed species and effectively remove unwanted species, such as carbonaceous deposits, from the catalyst surface, thereby rejuvenating its catalytic performance [14]. Using only CO₂ without plasma after the DRM reaction can eliminate carbon deposits by forming CO, but it needs a higher temperature, like 700 °C [15]. On the other hand, plasma can do the same coke oxidation by CO2 at lower temperatures, as analyzed in this work. Several researchers have explored the enhancement of catalyst performance through surface modification via pre-plasma treatment [16-19]. Previous studies have explored various shaped control catalysts, but no consistent trend was identified, indicating that the surface reaction mechanism relies on multiple catalyst properties. Our hypothesis suggests that employing shaped-controlled CeO2 in a plasma DRM environment can harness the morphology effect, and the active involvement of CeO2 introduces a novel layer to the surface reaction mechanism, enhancing overall performance.

The surface structure and exposed crystallographic planes of CeO₂ play a crucial role in determining its oxygen storage capacity and reactivity. Specifically, certain exposed planes, such as the (100), (110), and (111) stable planes [20], have been shown to exhibit higher concentrations of oxygen vacancies and enhanced redox properties as we investigated previously [21–29]. The surface energy of the planes is ranked as (111) < (110) < (100), while the energy required to form oxygen vacancies follows the order (110) < (100) < (111) [30]. By incorporating plasma assistance in the DRM process, we aimed to further modify the surface properties, such as oxygen vacancy generation of the CeO2 supports. This study delves into the effect of CeO2 support morphology on NiOx-CeO2 interactions and their consequential impact on catalytic performance within a DBD plasma-assisted DRM environment, focusing on harnessing low-temperature (<500 °C) catalytic capabilities. Our study uniquely investigates the impact of plasma addition on NiO_x-CeO₂-shaped catalysts, examining changes in reaction selectivity, catalyst structure, and coke formation. Furthermore, we investigate the degradation in the catalytic performance of the shaped catalyst following multiple DRM reactions and subsequent regeneration through coke gasification. Through a comprehensive analysis of catalytic activity under diverse temperature and plasma power conditions, employing NiOx-CeO2 nano-cubes and nano-octahedra catalysts in a plasmaassisted environment, we aim to provide valuable insights into the influence of support shape and plasma assistance on oxygen vacancy creation, redox characteristics, and overall catalytic performance in lowtemperature DRM processes.

2. Experimental section

2.1. Shaped catalyst synthesis

2.1.1. Synthesis of CeO₂ nanostructures

As previously reported [31–33], the synthesis of CeO₂ supports involved modified hydrothermal and coprecipitation methods. A seed-mediated hydrothermal method was employed to obtain the CeO₂ nano-cubes (NC) support. A 88 mL solution of 0.1 M Ce(NO₃)₃·6H₂O (Acros Organics, 99.5 %) was vigorously stirred while adding 6.0 M NaOH (VWR, 99 %) solution (8 mL) dropwise. The resulting mixture was stirred for approximately 30 s, then sealed in a stainless steel autoclave, placed in a box oven, and maintained at 150 °C for 48 h to achieve the desired CeO₂ NC morphology. The obtained sample underwent washing with deionized (DI) water (around 700 mL) to eliminate Na⁺ ions, followed by an ethanol wash (around 20 mL) to prevent hydrogen bonding formation. After drying at 80 °C for 24 h, the sample was grounded using a mortar and pestle to obtain the CeO₂ NC powder support.

A simple coprecipitation method was utilized to synthesize the CeO $_2$ nano-octahedra (NO) support. The precipitating agent NH₄(OH) (VWR Chemicals BDH, 28 - 30 %) and precursor Ce(NO $_3$) $_3\cdot$ 6H $_2$ O (Acros Organics, 99.5 %) were employed as the starting materials. The process involved the slow dropwise addition of a 1.0 M NH₄(OH) solution to a room temperature 0.1 M Ce(NO $_3$) $_3\cdot$ 6H $_2$ O solution, followed by homogenization through magnetic stirring at approximately 70 °C for 1 h on a hotplate. The resulting CeO $_2$ precursor was washed with DI water and then dried at 80 °C for 24 h to remove residual ions and water content. Subsequently, the dried sample underwent grinding with a mortar and pestle and was further calcined at 700 °C for 2 h in a box oven to obtain the final CeO $_2$ NO-shaped powder support.

2.1.2. Synthesis of Ni-doped CeO2 shaped catalyst

A coprecipitation method described in our prior work [26,33,34] was employed to synthesize the NiOx-CeO2 catalysts. In this method, the CeO2 NC and NO support powders were exclusively mixed with DI water in separate beakers, and the mixtures were stirred at approximately 60 °C. A 1.0 M aqueous solution of NH₄(OH) and an aqueous precursor solution of Ni(NO₃)₂·6H₂O were simultaneously added gradually to the mixtures of CeO2 and DI water while upholding a pH range of 9.0 to 9.5 for each solution. The resulting precipitated solutions were homogenized at around 60 °C for 24 h. Subsequently, the solutions were filtered and thoroughly washed using DI water and ethanol. After washing, the samples were dried at 80 °C for 20 h to eliminate leftover moisture, resulting in solid solutions of Ni-doped CeO2. The obtained solidsolutions were meticulously grounded into a fine powder through hand mortar and pestle. These powders were then subjected to calcination at 450 °C for 6 h in a box furnace, resulting in the desired final catalysts comprising CeO2 NC and NO supported with NiOx-based nanoparticles. The catalysts obtained had a 10 wt% of Ni loading and, thus, were labeled as 10 wt% Ni-CeO₂ NC and 10 wt% Ni-CeO₂ NO.

2.2. Catalyst characterization

XRD analysis was utilized in a Philips X'Pert MPD diffractometer with Cu K α radiation ($\lambda=1.5418$ Å) at 40 kV and 40 mA. Diffraction angles (20) were measured between 10° and 90° , and patterns were compared to the powder diffraction file (PDF) database for crystallographic information.

A FEI Tecnai F20 TEM, operating at 200 kV, was used for highresolution TEM imaging to examine particle shape and size. A JEOL 7000F SEM, operating at an acceleration voltage of 30 kV equipped with an EDS detector, was employed to investigate the synthesized samples' particle agglomeration and chemical compositions. For SEM-EDS characterization, carbon tape was used for fresh catalysts, while aluminum tape was used for spent catalysts due to the presence of carbon in the spent samples. The Ni doping concentration in CeO₂ was quantified using an Agilent 8900 OOO-ICP-MS.

Non-destructive Raman spectroscopy characterization of catalysts was conducted using a Horiba LabRAM HR 800 Raman spectrometer with a 100-long working distance objective (N_A=0.60). The Raman spectra were obtained in the 100 to 1800 cm $^{-1}$ range with a wavelength (λ) of 532 nm for excitation.

XPS data were acquired using a Kratos Axis Ultra DLD spectrometer with a monochromatic Al K α source (hv = 1486.6 eV), and the obtained spectra were processed and deconvoluted using CASA XPS software.

The powder samples' specific surface area was determined using the BET method by measuring nitrogen (N2) adsorption and desorption isotherms at approximately 78 K. The data were recorded using a thermal conductivity detector (TCD) integrated within a Micromeritics AutoChem II 2920 chemisorption analyzer. The reducibility and metalsupport interaction of the powder samples were analyzed through H₂ temperature programmed reduction (H2-TPR) experiments using the same AutoChem II 2920 chemisorption analyzer. A gas mixture of 10 vol % H₂ and 90 vol% Ar (flow rate: 50 mL/min) was used with temperatures ranging from 30 to 900 °C. CO2 temperature programmed desorption (TPD) experiments were conducted to study adsorption-desorption behavior and the presence of basic sites in the synthesized catalysts. The desorption of CO₂ at elevated temperatures was monitored using TCD of AutoChem II 2920 chemisorption analyzer under a helium atmosphere. Both H₂-TPR and CO₂-TPD experiments utilized samples weighing approximately 90 mg.

2.3. Catalytic performance evaluation

2.3.1. Experimental setup and conditions

The DRM performance of the synthesized catalysts was evaluated using a coaxial tube fixed-bed flow DBD reactor system described in our previous work [33,34] and supplementary section S1. The DRM process performance was evaluated by analyzing the gas species measured in the DBD plasma experimental system. For each set experiment, a catalyst weighing around 200 mg was placed and distributed within quartz wool (dielectric constant of 3.76) in the DBD reactor section. The catalyst was not subjected to additional reduction or oxidation treatment after calcination at 450 °C for 6 h, ensuring that NiO_x species remained as the primary active sites. The catalysts' performance was investigated under varying thermal energy and plasma power to understand their impact on catalytic performance and underlying mechanisms. The temperature analyzing range in this study was 150-450 °C, and the plasma power range was 8.3 - 27.1 W while keeping a moderate constant flow of 350 sccm ($CH_4:CO_2 = 150:250 = 0.4$). To calculate average plasma power, the obtained voltage and current waveforms from the oscilloscope were used according to the methodology described in the literature [35]. Fig. S1 displays typical waveforms of voltage and current applied during plasma catalysis, while Fig. S2 illustrates the Lissajous curve employed for power calculation. The catalyst underwent plasma-assisted DRM in each experiment cycle for 15–20 min, where a mixture of CH₄ and CO₂ flowed into the reactor. In post-reaction, the reactor was purged with Ar to eliminate residual gases, followed by catalyst regeneration for 30-35 min with Ar and CO₂ in a plasma environment. This procedure aimed to uphold consistent catalyst conditions after each reaction. For each data point, a minimum of three observations were collected and used for further analysis. Fig. S3 provides the recorded raw data from the quadrupole mass spectrometer (QMS) system for reference.

2.3.2. Experimental performance assessment

The performance assessment of the DRM experiment involved the consideration of the following parameters:

Conversion: Reactant conversion refers to the fraction of reactants that undergo the desired reaction. The conversions of CH₄ and CO₂ can be calculated using **Equations (1) and (2)**, respectively.

$$CH_{4}\,conversion = \\ \left[\frac{CH_{4}\,consumed\,(moles)}{CH_{4}\,supplied\,(moles)} \right] \times 100\% \tag{1}$$

$$CO_{2} \, conversion = \, \left[\frac{CO_{2} \, consumed \, (moles)}{CO_{2} \, supplied \, (moles)} \right] \times 100\% \tag{2}$$

Yield: Yield determines the efficiency of a specific reaction by measuring the ratio of the produced products to the input reactants involved. The product yields of CO and H_2 can be determined using **Equations (3) and (4),** respectively.

$$CO\,yield = \left[\frac{CO\,produced\,(moles)}{CH_{4}\,and\,CO_{2}\,supplied\,(moles)}\right] \times 100\% \tag{3}$$

$$H_{2}\,\text{yield} = \\ \left[\frac{H_{2}\,\text{produced}\,(\text{moles})}{2 \times \text{CH}_{4}\,\text{supplied}\,(\text{moles})} \right] \times 100\% \tag{4}$$

Selectivity: Selectivity quantifies the percentage of undesired products generated in conjunction with the desired ones, considering the reactants consumed. The product selectivity of CO and H_2 can be calculated using **Equations (5) and (6)**, respectively.

$$\mbox{CO selectivity} = \\ \left[\frac{\mbox{CO produced (moles)}}{\mbox{CH}_4 \mbox{ and } \mbox{CO}_2 \mbox{ consumed (moles)}} \right] \times 100\% \tag{5}$$

$$H_{2}\, selectivity = \\ \left[\frac{H_{2}\, produced \, (moles)}{2 \times CH_{4}\, consumed \, (moles)} \right] \times 100\% \tag{6}$$

Carbon Balance and H_2/CO Ratio: The carbon balance assesses the unbalanced carbon in different forms, while the H_2/CO ratio offers insights into the proportion of products relative to each other. Carbon balance is calculated using **Equation** (7), and the H_2/CO ratio is determined using **Equation** (8).

$$\mbox{Carbon balance} = \\ \left[\frac{(\mbox{CO} + \mbox{CO}_2 + \mbox{CH}_4) + 2 \times \mbox{ } \mbox{C}_2\mbox{H}_6(\mbox{moles})}{\mbox{CH}_4 \mbox{ and } \mbox{CO}_2 \mbox{ supplied (moles)}} \right] \times 100\% \label{eq:CH_4}$$

$$\frac{H_2}{CO} = \left[\frac{H_2 \text{ produced (moles)}}{CO \text{ produced (moles)}} \right]$$
 (8)

Specific Energy Input (SIE) and Energy Efficiency (EE): SIE quantifies the applied plasma energy on the feed gas to maintain plasma. EE measures the consumption of feed gas per unit of plasma energy. SIE is calculated using **Equation** (9), and EE is determined using **Equation** (10).

$$SIE\left(kJ/sccm\right) = \left[\frac{Measured\ plasma\ power\left(W\right)\times 60}{Feed\ gas\ flow\ rate(sccm)\times 1000}\right] \tag{9}$$

$$EE\left(\frac{mmol}{kJ}\right) = \left[\frac{CH_{4} \, and \, CO_{2} \, consumed \, (moles) \, per \, minute \, \times \, 10^{6}}{Measured \, plasma \, power \, (W) \, \times \, 60}\right] \tag{10} \label{eq:energy}$$

3. Results and discussion

3.1. Structural and morphological analysis

3.1.1. XRD and BET surface area

The crystal structures of the synthesized samples were analyzed through XRD analysis presented in Fig. 1. Both CeO_2 NC and NO supports, along with Ni-doped 10 wt% Ni- CeO_2 catalysts, maintain a face-centered cubic fluorite structure (PDF# 34–0394) [31] with no structural changes upon Ni doping as observed in the XRD patterns. The XRD patterns of fresh 10 wt% Ni- CeO_2 NC and NO catalysts in Fig. 1(a) show three distinct diffraction peaks at 37.1°, 43.3°, and 62.9°, corresponding to the (111), (200), and (220) planes of cubic NiO phase (PDF#

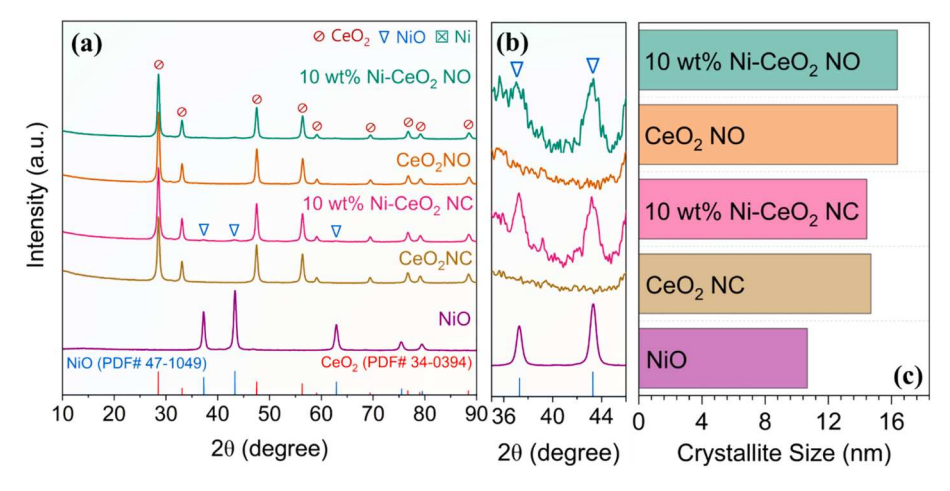


Fig. 1. XRD pattern of (a) fresh CeO2 supports, NiO, and 10 wt% Ni-CeO2 catalysts (b) magnified XRD pattern, (c) average crystallite size variation.

47–1049), confirming the presence of doped Ni in NiO form. The low-intensity NiO peaks shown in Fig. 1(b) are possibly due to a uniform dispersion of Ni on both CeO₂ NC and NO supports [36,37] and lower Ni loading. The XRD pattern of the pure NiO as a reference catalyst in Fig. 1 (a) confirms the presence of the cubic NiO phase, as evidenced by matching crystal planes with the database (PDF# 47–1049).

The crystallite sizes of the CeO_2 support and 10 wt% Ni- CeO_2 catalysts, calculated using the Scherrer equation considering different peaks are listed in Table 1. Almost no change in crystallite size is observed upon Ni incorporation on both CeO_2 -supported catalysts. The 10 wt% Ni- CeO_2 NO catalyst exhibits a larger crystallite size in each plane direction compared to the 10 wt% Ni- CeO_2 NC catalyst. The crystallite size values in each catalyst are pretty close across all three plane directions, suggesting that a mixture of all facets should be exposed on the catalysts' surfaces based on the literature [38]. However, HRTEM analysis reveals that both catalysts exhibit a combined mixture of (100) and (111) facets, but the relative proportion differs. Among them, the (100) facet is more prominent in the 10 wt% Ni- CeO_2 NC-shaped catalyst, whereas the 10 wt% Ni- CeO_2 NO-shaped catalyst shows more exposure of (111) facets

The specific surface areas of the supports and catalysts, listed in Table 1, offer insights into the metal-support interaction. The CeO $_2$ NC support (34.19 m 2 /g) exhibits a higher BET surface area compared to CeO $_2$ NO support (19.03 m 2 /g), likely due to differences in nanoparticle sizes, agglomeration, and morphology [39]. In the case of both CeO $_2$ -shaped catalysts, the BET surface area slightly increases after Ni doping. This substantial increase in specific areas for the catalysts indicates excellent dispersion of Ni and possibly promotes increased porosity in the support material [36,40].

Table 1Crystallographic information, surface area, and defect concentrations for all supports and catalysts.

Sample	Crystallite Size (nm) ^a			Specific Surface Area	$I_{\delta}/$
	(200)	$(220) (111) (m^2/g)^b$		I_{F2g}^{c}	
CeO ₂ NC	14.86	15.92	14.36	34.19	0.16
10 wt% Ni-CeO ₂ NC	14.69	15.94	14.28	37.02	0.20
CeO ₂ NO	15.26	16.50	16.23	19.03	0.11
10 wt% Ni- CeO ₂ NO	15.22	16.30	16.24	22.02	0.19
NiO	10.67			16.44	

^a Calculated using Scherrer equation; ^b surface area measured using single point BET method; ^c Calculated from Raman spectra considering δ and F_{2g} peak intensity.

3.1.2. TEM and SEM-EDS

Fig. 2 represents TEM images illustrating the morphologies of the supports for both fresh 10 wt% Ni-CeO $_2$ NC and NO catalysts. In Fig. 2 (a), the TEM image illustrates the cubic morphology of the 10 wt% Ni-CeO $_2$ NC catalyst, with side lengths between 6 and 17 nm. The subsequent HRTEM analysis depicted in Fig. 2(b) identifies the (200) facet, with a measured d-spacing of 0.28 nm, confirming that the exposed facets are predominantly (100). Although the (100) facet is the most visible, traces of the (111) facets are also observed with a d-spacing of 0.32 nm, indicating a mix of both facets in the 10 wt% Ni-CeO $_2$ NC catalyst.

The TEM images in Fig. 2(c) and 2(d) display the octahedral morphology of the 10 wt% Ni-CeO2 NO catalyst, with side lengths ranging from 8 to 23 nm. The observed octahedral shape is defined by both (111) and (100) facets, suggesting the structure may approach a truncated octahedral form [40]. In this catalyst, the (111) facets are more prominently exposed compared to the (100) facets. This configuration resembles a truncated octahedron, where most of the surface area is covered by the (111) facets, with only a smaller portion covered by the (100) facets. The variations in sizes (side lengths) or growth of each shape observed in the NC and NO may be attributed to non-uniform temperatures in the solutions during the hydrothermal and precipitation synthesis. The NiO particles in the TEM images are barely visible. The reason could be attributed to either the incorporation of Ni into the CeO2 lattice or significantly smaller NiO particles with high dispersion throughout the CeO₂ supports. The presence of NiO particles within CeO₂ support is evidenced in Fig. S4, with size ranges between 5 and 7 nm for both catalysts.

The SEM images and EDS elemental distributions of both fresh 10 wt % Ni-CeO $_2$ catalysts are presented in Fig. 3. The images and mapping show that both shaped catalysts exhibit agglomeration, with nickel being distributed fairly uniformly on the CeO $_2$ supports. Comparing both catalysts, nickel is more evenly spread in the 10 wt% Ni-CeO $_2$ NC sample, while in the NO sample, it appears in clusters. The EDS spectral analysis of both fresh catalysts in Fig. S5 reveals a consistent composition of approximately 10 wt% Ni for each shaped catalyst. The elemental composition was further verified using Inductively Coupled Plasma Mass Spectrometry (ICP-MS) analysis, and the results, along with the sample preparation method, are presented in Table S1. The measured weight percentage of Ni was approximately 7 wt%, which is lower than the intended synthesized amount.

3.2. Spectroscopic analysis

3.2.1. Raman analysis

The Raman spectra in Fig. 4 illustrate point defects, bonding, and

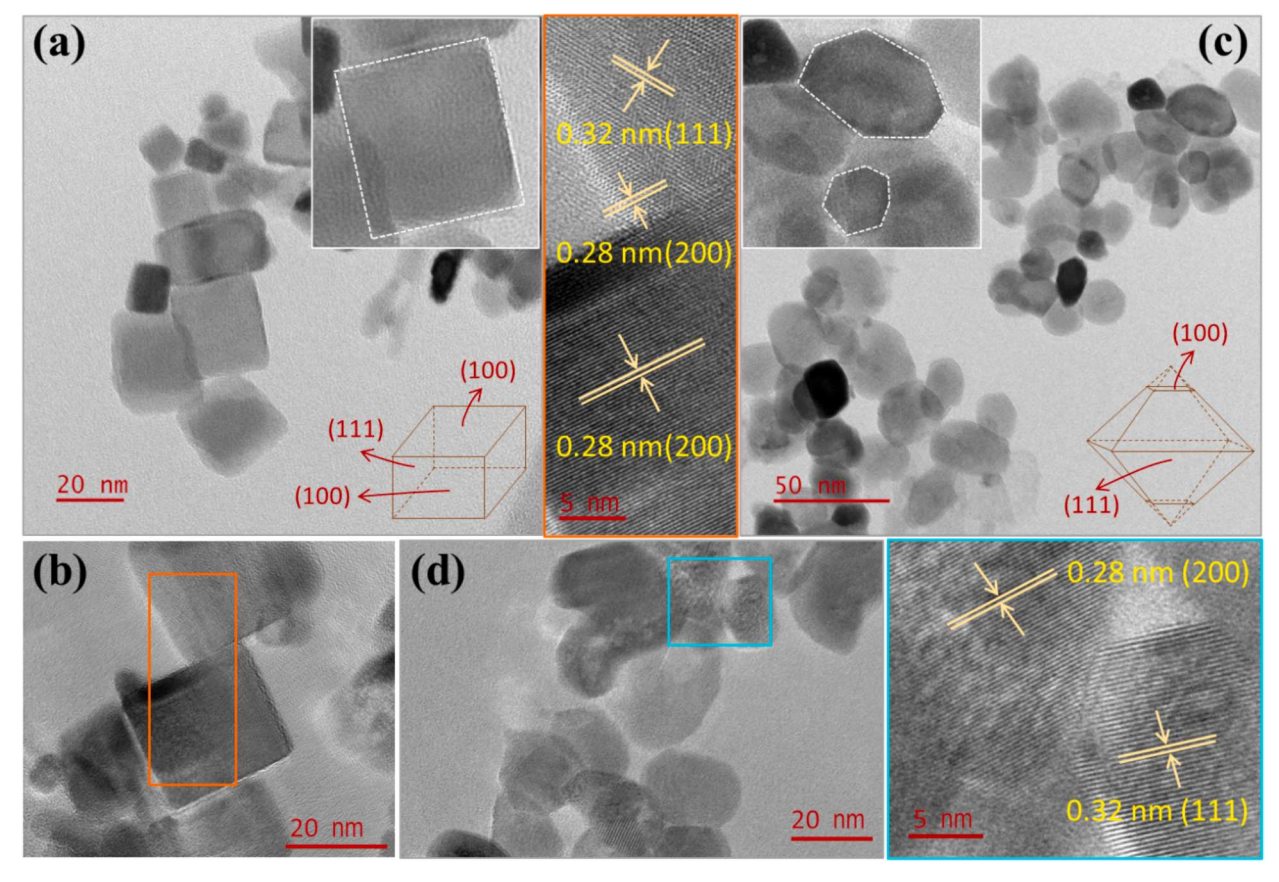


Fig. 2. TEM and HRTEM images of (a, b) 10 wt% Ni-CeO2 NC (c, d) 10 wt% Ni-CeO2 NO catalyst representing catalyst shapes and exposed facets.

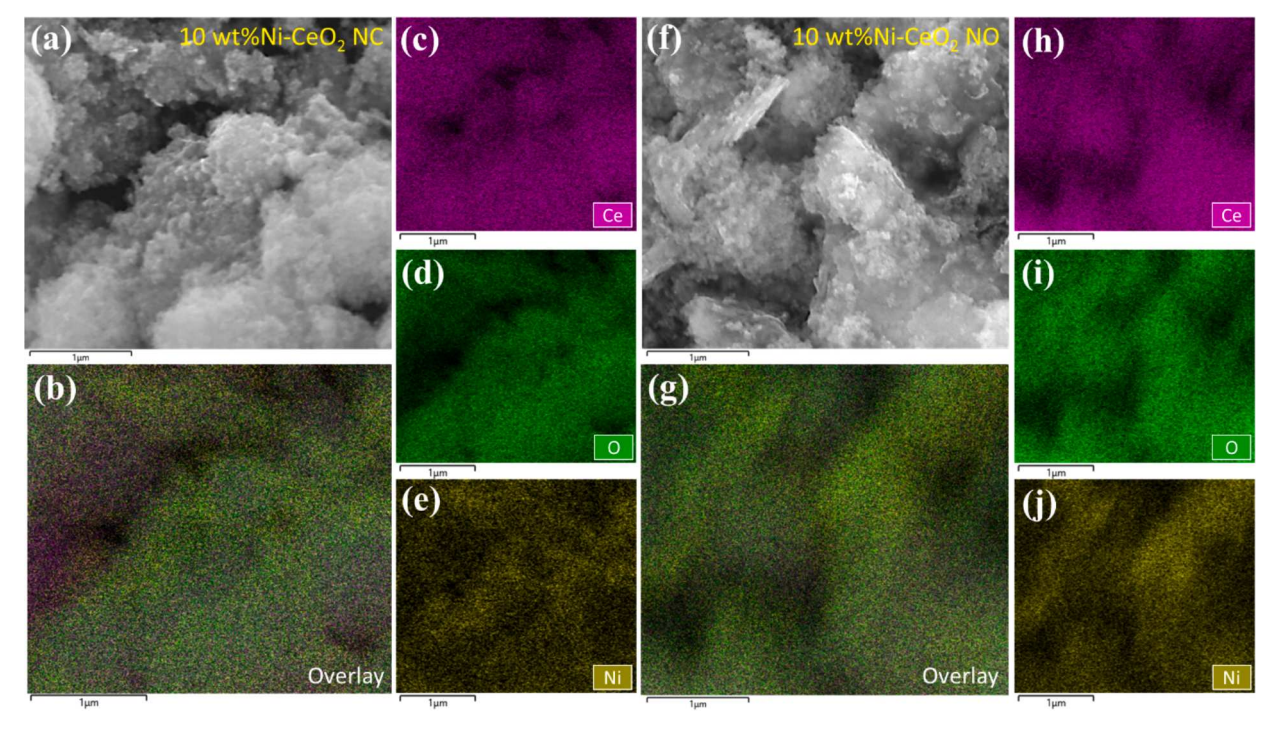


Fig. 3. SEM image, EDS layered image, and elemental mapping of (a - e) 10 wt% Ni-CeO₂ NC (f - j) 10 wt% Ni-CeO₂ NO catalyst exhibiting the elemental distribution of Ni over CeO₂ supports.

lattice distortion for both ${\rm CeO_2}$ supports and the fresh 10 wt% Ni-CeO $_2$ catalysts. In both pristine ${\rm CeO_2}$ NC and NO supports, the peak around 463 cm $^{-1}$ corresponds to the symmetric stretching of oxygen atoms

within the fluorite lattice, F_{2g} [25,27]. Upon Ni incorporation, this peak shifts downward to 447 cm $^{-1}$ in 10 wt% Ni-CeO $_2$ NC and 445 cm $^{-1}$ in 10 wt% Ni-CeO $_2$ NO catalyst, indicating structural distortion and lattice

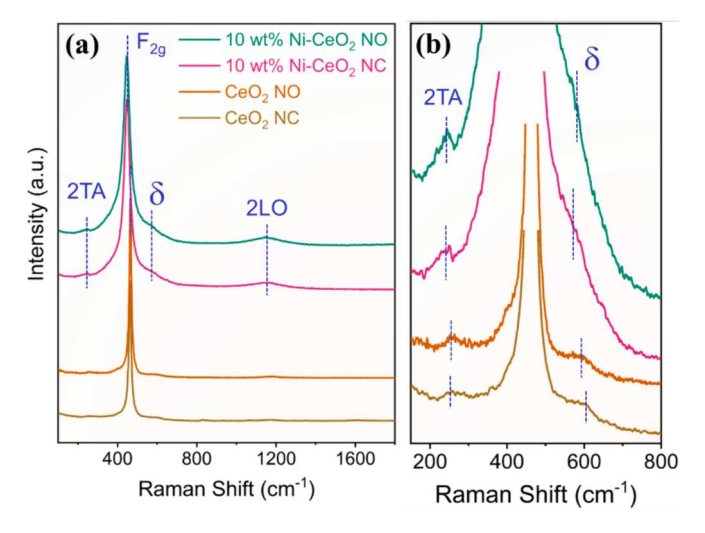


Fig. 4. (a) Raman spectra of ${\rm CeO_2}$ support, fresh 10 wt% Ni-CeO₂ catalysts (b) magnified spectra.

expansion. The downward frequency shift is directly correlated with lattice strain and distortion [41], with 10 wt% Ni-CeO2 NO exhibiting more pronounced lattice distortion. Additionally, all supports and catalysts observed a defect-induced peak (δ) associated with the vibrational modes of oxygen atoms surrounding vacancy sites [21]. Oxygen vacancy/point defect is associated with this peak, as oxygen vacancies are generated to maintain charge balance upon substituting Ce⁴⁺ or Ce³⁺ with Ni^{2+} [42]. These vacancy sites are highly active in catalysis. The δ peak position shifted from 597 to 563 cm⁻¹ for the NC shape and from 590 to 567 cm⁻¹ for the NO shape, indicating a change in oxygen vacancy/point defects. The corresponding intensity ratio of δ and $F_{2\sigma}$ peak provides information about the relative amount of point defects in the catalysts [43], as listed in Table 1. The data in the table clearly indicates that the incorporation of Ni increases the point defect concentration in both 10 wt% Ni-CeO2 catalysts, with a more pronounced effect or changes observed in the 10 wt% Ni-CeO₂ NO-shaped catalyst. Here, the extent of point defect increasing with Ni incorporation is intricately linked to the catalyst's morphology/exposed facets. Shifting other peaks in the catalysts, such as TA (transverse acoustic phonon mode) and 2LO (second-order longitudinal optical phonon mode), confirm the structural modifications possibly influenced by the presence of NiOx in the CeO2 lattice.

3.2.2. XPS analysis

XPS investigations were conducted to analyze the elements' chemical composition and oxidation states on the catalyst surfaces. The XPS spectra of Ce 3d, O 1s, and Ni 2p were examined for both 10 wt% Ni-CeO₂ catalysts as depicted in Fig. 5. The Ce 3d XPS spectra in Fig. 5(a) exhibits characteristic peaks, including v^0 , v, v', v'', v''', u^0 , and u, corresponding to binding energies (BEs) of approximately 880.6, 882.6, 885.4, 888.8, 898.4, 898.9, and 901 eV, respectively, in both shaped catalysts [27,44]. Among these peaks, v^0 , v', and u^0 represent Ce³⁺ states, while the remaining peaks represent Ce⁴⁺ states. The relative concentration of Ce³⁺ species, presented in Table 2, exhibits a higher abundance of Ce³⁺ species (34.35 %) with the NO catalyst compared to the NC catalyst (24.90 %). The higher Ce³⁺ concentration indicates the catalysts' redox functionality strength, ultimately contributing to the DRM performance.

The O 1s peaks shown in Fig. 5(b) provide a clearer understanding of the oxygen vacancy concentration. The deconvolution of the O 1s peaks reveals three distinct peaks representing lattice oxygen (O_L) , oxygen vacancy (O_V) , and chemisorbed oxygen (O_C) [22,31]. The BEs for these peaks are similar for both 10 wt% Ni-CeO $_2$ catalysts, except for a shoulder peak at a higher BE observed in the NO catalyst sample, contributing to the oxygen vacancy (O_V) concentration. The relative amount of oxygen vacancy is higher in the NO catalyst (23.75 %) compared to the NC catalyst (18.12 %), which correlates with more active sites for catalytic reaction, specifically CO_2 adsorption and dissociation [36,45].

The analysis of Ni 2p states in Fig. 5(c) provides insights into the active states of Ni, which play a crucial role in the CH₄ conversion as CH₄ is typically adsorbed on Ni sites [46,47]. The deconvolution of the Ni 2p peaks reveals two oxidation states, Ni²⁺ and NiO, along with the satellite peak [48]. The NiO peak corresponds to the surface NiO dispersed throughout the support, indicating weak interactions with the support. On the other hand, the Ni²⁺ peak represents Ni species interacting strongly with the CeO₂ lattice [49,50], providing more active sites for CH₄ adsorption. The ratio of Ni²⁺ to NiO indicates the strength of metal-

 Table 2

 Relative compositions of elements from XPS analysis.

Sample	Ce ³⁺	Ce ⁴⁺	O_L	O _V	O _C	Ni ²⁺ / NiO
10 wt% Ni- CeO ₂ NC	24.90 %	75.1 %	80.81 %	18.12 %	1.07 %	1.76
10 wt% Ni- CeO ₂ NO	34.35 %	65.65 %	76.20 %	23.75 %	0.05 %	2.25

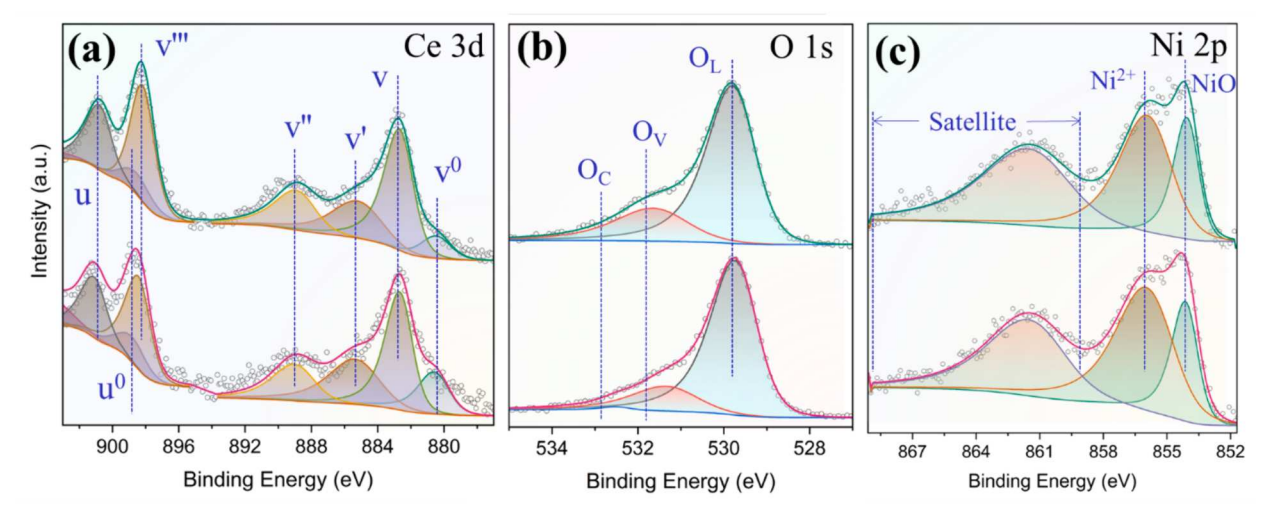


Fig. 5. XPS analysis of (a) Ce 3d, (b) O 1s, and (c) Ni 2p for 10 wt% Ni-CeO2 NO (top spectra) and 10 wt% Ni-CeO2 NC (bottom spectra) catalysts.

support interactions [50] and the availability of active sites for CH_4 adsorption, and it is higher for the NO catalyst, as shown in Table 2. The observed little variations in peak intensities and BEs for all elements between catalysts in Fig. 5(a-c) provide evidence of distinct surface chemistries and oxidation states which suggest distinct electronic interactions between the CeO_2 support shapes and the NiO_x active species.

3.3. Temperature-programmed chemisorption analysis

3.3.1. H₂-TPR

The reducibility and interaction between NiO_x and CeO_2 in the synthesized catalysts were explored using H_2 -TPR experiments, as the catalysts' ability to undergo reduction and reoxidation cycles is crucial. The H_2 -TPR profiles depicted in Fig. 6(a) display the H_2 consumption peaks for CeO_2 supports, 10 wt% Ni-CeO $_2$ catalysts, and pure NiO. Both the CeO_2 NC and NO supports exhibit two prominent peaks, with one occurring between $450-550\,^{\circ}\mathrm{C}$ (γ) attributed to the reduction of surface CeO_2 into $CeO_{2\text{-x}}$, and the other between $700-800\,^{\circ}\mathrm{C}$ (δ) corresponding to the bulk reduction of CeO_2 from Ce^{4+} to Ce^{3+} [21,51].

The profiles of the 10 wt% Ni-CeO₂ NC and NO catalysts exhibit reduction peaks in the temperature ranges of 150 – 250 °C, 250 – 350 °C. and $700-800\,^{\circ}$ C. The first two peaks in the $150-250\,^{\circ}$ C range, referred to as α_1 and α_2 , are associated with the reduction of highly dispersed NiO species exhibiting weak interactions with the support [52,53]. Notably, the 10 wt% Ni-CeO2 NC catalyst shows relatively lower temperature adsorbed peaks (188 °C and 213 °C) compared to the 10 wt% Ni-CeO₂ NO catalyst (191 $^{\circ}$ C and 240 $^{\circ}$ C). The very intense peak, β , in the range between 250 – 350 $^{\circ}$ C is attributed to the formation of solid solutions between NiO_x and CeO₂. This suggests a strong interaction between the components, possibly in the form of NiOx-doped CeO2 and/or CeO2doped NiO_x. The presence of NiO in the catalysts facilitates the reduction of surface CeO₂, particularly the Ce⁴⁺ ions, leading to a downward shift of the β peak to lower temperatures [54]. It is significant to highlight that the NiO reduction peaks for both catalysts are below 350 °C, whereas pure NiO exhibits a reduction peak above 350 °C, as shown in Fig. 6(a).

The reduction peak, δ , observed at a high temperature between 700 - 800 $^{\circ}\text{C}$ indicates the bulk reduction of CeO2. After Ni impregnation, both catalysts show a decrease in this peak temperature, suggesting a modification in the redox properties. The overall H_2 consumption, as indicated in Table 3, reveals that the 10 wt% Ni-CeO2 NO catalyst (1902.12 $\mu\text{mol/g})$ demonstrates elevated H_2 consumption, suggesting superior reducibility and potentially more active sites compared to the 10 wt% Ni-CeO2 NC catalyst (732.43 $\mu\text{mol/g})$.

Table 3 $$\rm H_2\,consumption~from~H_2\text{-}TPR~and~basic~sites~from~CO_2\text{-}TPD~analysis~of~supports~and~catalysts.}$

Sample	H ₂ Consumption	Basic sites (µmol/g)			
	(μmol/g)	Weak (100 – 300 °C)	Moderate (300 – 500 °C)	Strong (500 – 900 °C)	
CeO ₂ NC	397.29	111.97	397.36	158.41	
10 wt% Ni- CeO ₂ NC	732.43	96.61	191.25	311.76	
CeO ₂ NO	423.52	61.43	110.52	150.57	
10 wt% Ni- CeO ₂ NO	1902.12	32.29	143.84	97.28	
NiO	8780.77	68.60	186.20	375.32	
Ni	_	34.61	109.70	39.03	

3.3.2. CO₂-TPD

CO2-TPD experiments were conducted to investigate the adsorption and desorption behavior of CO2 on the catalyst surfaces, providing insights into their surface basicity. The experimental TPD profiles in Fig. 6 **(b)** reveal three distinct sections: weak basic sites $(100 - 250 \, ^{\circ}\text{C})$, moderate basic sites (250 - 500 °C), and strong basic sites (500 -900 °C) [41]. These sites correspond to bicarbonate bonding, bidentate carbonates, and monodentate carbonates [26]. The quantitative analysis presented in Table 3 provides the respective strengths of these sites for CeO2 supports, 10 wt% Ni-CeO2 catalysts, pure NiO, and Ni. Previous studies suggest that catalyst oxygen vacancies adsorb CO2 by integrating oxygen atoms into the vacancy sites [43,45], indicating a correlation between basic sites and oxygen vacancies. In the experimental trend shown in Fig. 6(b), both CeO₂ supports and catalysts exhibited all types of basic sites. It is known that weak and moderate basic sites are vital for CO2 adsorption and desorption at lower temperatures, while strong basic sites form stronger bonds between the CO2 and catalyst surface, promoting coke formation [41,55]. In Table 3, it is evident that the CeO₂ NC support initially has a higher proportion of moderate basic sites compared to stronger basic sites. However, Ni doping in the CeO2 NC support increases the strength of strong basic sites and decreases the strength of moderate basic sites in the 10 wt% Ni-CeO₂ NC catalyst. This shift is likely due to the presence of more NiO particles in the catalyst, as pure NiO contributes more to strong basic sites, as mentioned in Table 3 and NiO deconvolution in Fig. S6. On the other hand, when Ni is doped into the CeO2 NO support, it increases the number of moderate basic sites, which is desirable for catalytic application. This increase could be attributed to Ni incorporation into the CeO2 lattice, as metallic Ni contributes more to moderate basic sites. The 10 wt% Ni-CeO2 NC catalyst

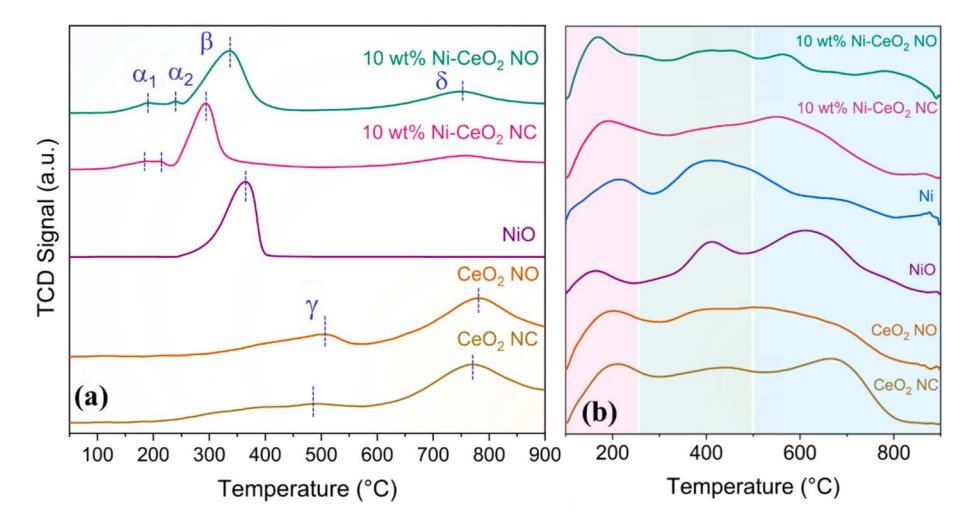


Fig. 6. (a) H2-TPR profiles of CeO2 supports, NiO, and 10 wt% Ni-CeO2 catalysts (b) CO2-TPD profiles of CeO2 supports, NiO, Ni, and 10 wt% Ni-CeO2 catalysts.

exhibits a significantly greater total number of basic sites compared to the 10 wt% Ni-CeO $_2$ NO catalyst, possibly due to its larger surface area. Despite the higher total number of basic sites in the 10 wt% Ni-CeO $_2$ NC catalyst, its contribution to catalytic performance may be limited due to the relatively higher presence of stronger basic sites. These findings align with observations of oxygen vacancies and defects through Raman and XPS analysis, indicating that the 10 wt% Ni-CeO $_2$ NO catalyst different interaction than the 10 wt% Ni-CeO $_2$ NC catalyst. The dissimilar peak intensities temperatures observed in the CO $_2$ -TPD profiles between catalysts indicate surface adsorption sites' strength and quantity variations.

3.4. Plasma-assisted DRM performance evaluation

3.4.1. Thermal effect on performance

Fig. 7 illustrates the effects of temperature on the DRM performance of using 10 wt% Ni-CeO₂ NC and NO catalysts. The experiments were conducted at temperatures ranging from 150 to 450 °C, with/without a constant plasma power of approximately 23.8 W (± 1.1 W) and a CH₄ to CO₂ ratio of 0.4 (100 sccm/250 sccm). The performance of both pure thermal DRM (Fig. 7(a-d)) and plasma-assisted DRM (Fig. 7(e-i)) are presented in the figure. For the purely thermal DRM processes shown in Fig. 7(a), the conversion of reactants starts at about 350 °C and increases as the temperature rises. Between 350 and 450 °C, the CH₄ conversion rates for both catalysts remain essentially the same. However, at 450 °C, the CO₂ conversion rate shows a notable difference of about 6 % between the NC and NO catalysts. This variation can be linked to rich

oxygen vacancy concentration, which serves as active sites for CO_2 adsorption [41], highlighting a potential bifunctional reaction mechanism at these sites. The influence of oxygen vacancy on CO_2 activation was examined by Niu J. et al. [45] using DFT simulations and discussed in a review by Rosli S. et al. [56], which includes several experimental studies.

In plasma-assisted DRM, as depicted in Fig. 7(e), both conversions commence at a lower temperature of 150 °C, with the NO catalyst exhibiting higher conversions compared to the NC catalyst. This verifies distinct plasma interactions with each shaped catalyst as a result of better conversion in NO catalysts. This enhanced activity in the NO catalyst may be attributed to a higher concentration of defects, either from lattice deformation or oxygen vacancy. As plasma micro-discharge formation on the catalyst surface, which increases performance by lowering gas breakdown voltage, is related to the defects of the catalysts [57]. Another notable finding is the consistent conversion rate differences (CH₄ or CO₂) between the catalysts beyond 300 °C. For instance, the catalysts have an approximate 8 % difference in CH₄ conversion between the 300 - 450 °C temperature range. This steady variance in conversions confirms the consistency in NiO_x-CeO₂ interactions between the catalysts within that temperature range.

The CO and $\rm H_2$ yields known as product efficiency shown in Fig. 7(f) for plasma DRM show a consistent trend with the conversions, with higher yields for the NO catalyst. One interesting observation is that for each catalyst (either NC or NO), the CO and $\rm H_2$ yield values remain close to each other in the 350 - 450 °C temperature region regardless of conversions. For example, at 450 °C, both CO and $\rm H_2$ yields for the NO

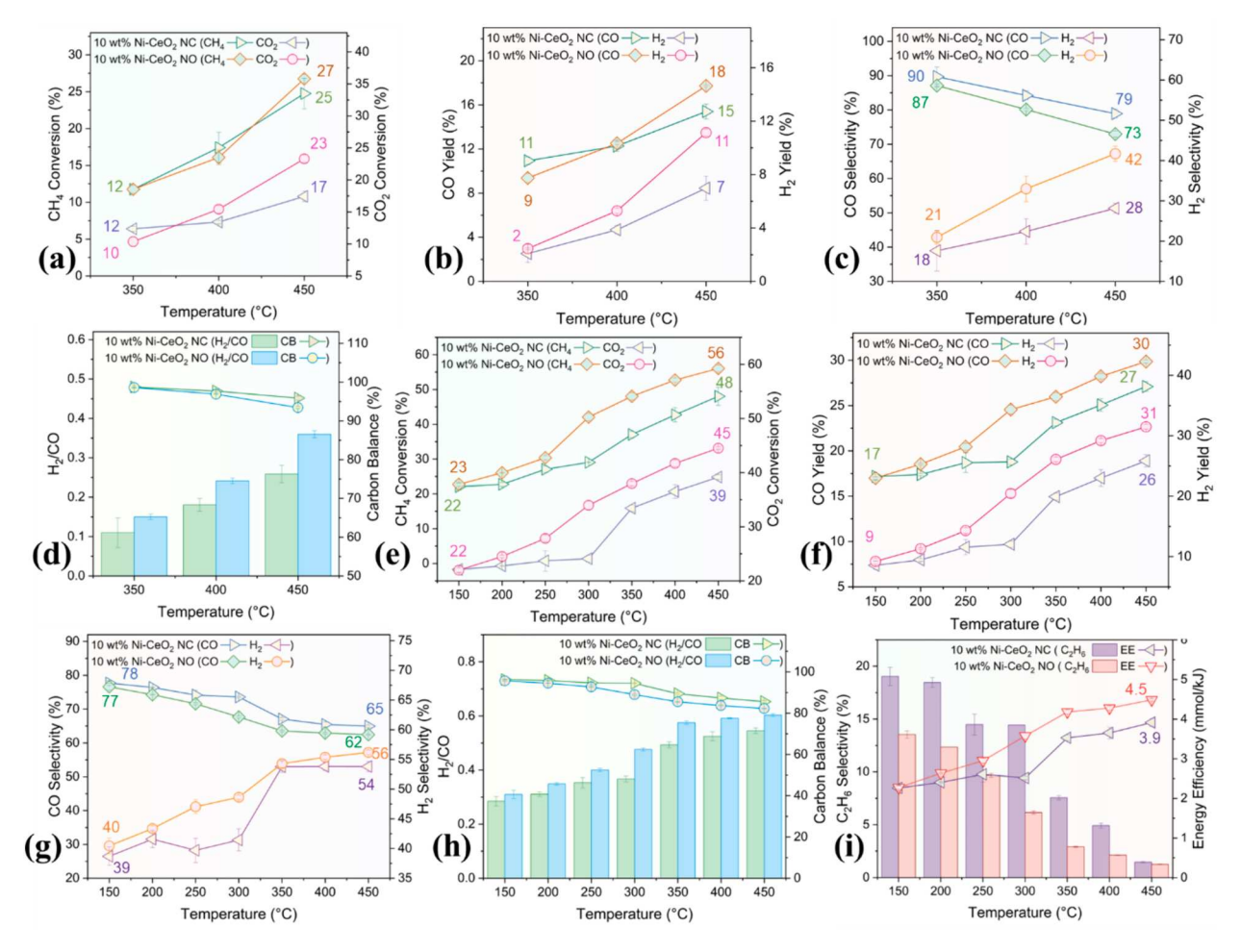


Fig. 7. Temperature effect on 10 wt% Ni-CeO $_2$ catalysts' performance under pure thermal DRM: (a) CH $_4$ and CO $_2$ conversion (b) CO and H $_2$ yield (c) CO and H $_2$ selectivity (d) H $_2$ /CO ratio and carbon balance; under plasma-assisted DRM: (e) CH $_4$ and CO $_2$ conversion (f) CO and H $_2$ yield (g) CO and H $_2$ selectivity (h) H $_2$ /CO ratio and carbon balance (i) C $_2$ H $_6$ selectivity and energy efficiency [Flow (sccm): CH $_4$ /CO $_2$ = 100/250 = 0.4, Power: 23.8 \pm 1.1 W, Temperature: 150 to 450 °C].

catalyst are approximately 30 %, while CH_4 and CO_2 conversions are 56 % and 45 %, respectively. This phenomenon highlights the catalyst's efficiency in converting CH_4 into CO and H_2 in the presence of plasma, considering the feed gas ratio is not unity. Liu et al. [79] observed similar effect where CH_4 reacted with lattice oxygen to produce CO. The observed identical CO and CO and CO phenomena in plasma-assisted DRM are not present in the pure thermal DRM yield, as shown in Fig. 7(b); instead, they follow their conversion trends.

The H₂/CO ratio is higher for plasma DRM compared to pure thermal DRM, as illustrated in Fig. 7(d) and 7(h). The reason could be the efficiency of plasma in breaking C-H bonds compared to C=O bonds since less energy is required to break C-H bonds [58]. Previous studies using different catalysts also observed this plasma effect in bond breaking [59-61]. Fig. 7(d) and 7(h) also show the unbalanced carbon calculation in different forms with temperature change. With increasing temperature, carbon deposition intensifies due to enhanced carbon deposition reactions like methane cracking ($CH_4 \rightarrow C + 2H_2$), Boudouard (2CO \rightarrow CO₂ + C), steam generation (CO₂ + 2H₂ \rightarrow C + 2H₂O), and CO reduction (CO + $H_2 \rightarrow C + H_2O$) [15,34]. The Boudouard, steam generation, and CO reduction reactions are spontaneous below 500 °C [62], potentially influencing both pure thermal and plasma-assisted processes. Conversely, although methane cracking is unfavorable below 500 °C, plasma addition may facilitate this reaction, leading to increased carbon deposition and H2 formation in plasma-assisted DRM environments. In the plasma environment (Fig. 7(h)), the carbon balance between 10 wt% Ni-CeO2 catalysts aligns at lower temperatures but diverges above 250 °C, which is consistent with conversion data. Typically, a higher conversion rate indicates an increase in the possibility of carbon formation reactions. The carbon is mostly deposited on the catalyst surface, which is further verified through Raman and EDS analysis later in this study. Despite substantial deposition, the carbon is highly reactive and readily gasified during plasma-assisted regeneration with CO₂, as presented in Fig. S3. Additionally, after regeneration, the catalyst's performance remained unchanged, indicating complete gasification of deposited carbon potentially through reverse Boudouard (CO₂ + C \rightarrow 2CO) reaction.

The overall reaction direction expressed through the selectivity trend in plasma-assisted DRM is illustrated in Fig. 7(g). The trend depicts increasing H2 selectivity and decreasing CO selectivity with rising temperatures for both catalysts. Initially, at lower temperatures (150 °C), favoring CO production is possibly attributed to the involvement of CH₄ with CeO₂ lattice oxygen (O') to produce CO. However, with the rise in temperature, other pathways promote H₂ formation favorably through the WGS reaction (CO+ $H_2O \rightarrow CO_2 + H_2$) pathway since it is favorable at lower temperatures [62]. At any temperature, the NO catalyst produces relatively more H2, while the NC produces more CO, showing the difference in product formation reactivity of both catalysts. The NC catalyst shows higher activity in producing C2H6, possibly through CH_4 to C_2H_6 ($2CH_4 \rightarrow C_2H_6 + H_2$) conversion, as shown in Fig. 7(g), indicating its preference for C₂H₆ formation. This C₂H₆ production declines with temperature and diverts the reaction towards H₂ production. A possible reason could be that the lowering activation barrier with rising temperatures facilitates the breakdown of C2H6 through ethane cracking ($C_2H_6 \rightarrow 2C + 3H_2$) and/or ethane dry reforming $(C_2H_6 + 2CO_2 \rightarrow 4CO + 3H_2)$ with plasma assistance.

The energy efficiency (EE) of both catalysts, considering the amount of plasma power consumed, is calculated and shown in Fig. 7(i). Since the furnace temperature is identical for both catalysts for each data point, calculating EE based on plasma power alone reasonably compares catalyst performance. At relatively lower temperatures ($<250~^\circ\text{C}$), the EE values for both catalysts are close to each other. However, at higher temperatures ($>250~^\circ\text{C}$), the differences become more pronounced as like conversion data, with the NO catalyst exhibiting higher EE of 4.5 mmol/kJ at 450 $^\circ\text{C}$. This suggests that higher temperatures are favorable for economic conversion for NO catalyst compared with NC catalyst.

3.4.2. Plasma power effect on performance

Plasma power effect on DRM performance at a constant temperature is utilized, and the results are shown in Fig. 8. In our previous study [33], we examined the impact of either plasma or catalyst individually where in both cases, the performance was lower than plasma-catalyst synergy. The applied plasma power for this study varied between 8.3 and 27.1 W at 350 °C temperature. Both CH₄ and CO₂ conversions increase with plasma power, as shown in Fig. 8(a). Increasing plasma power generally introduces more reactive species, which enhances the dissociation of CH₄ and CO₂. Similar to the thermal effects previously observed on the catalysts, the NO catalyst surpassed the NC catalyst in performance, achieving the highest conversion at the maximum plasma power applied. The superior conversion of the NO catalyst could likely be attributed to a better synergy between the catalyst and the plasma, possibly due to additional lattice defects and oxygen vacancy concentration compared to the NC catalyst. Previous studies indicated that increasing plasma power enhances the concentration of defects, creating more active sites or altering catalytic properties [63]. Later in this study, the spent catalyst characterization confirms the additional defects introduced after the plasma DRM reaction.

The catalysts' selectivity trends with plasma power are shown in Fig. 8(b), where CO selectivity decreases and $\rm H_2$ selectivity increases with increasing plasma power for both 10 wt% Ni-CeO₂ catalysts, aligning with the temperature effect trend observed in the previous section. A similar explanation could also be applicable here, such as CH₄ involvement in CO production at lower plasma power and increasing plasma power expediting WGS reaction. A crucial observation is that the catalyst's effectiveness in controlling the global reaction pathway remains consistent, whether the temperature is increased or the plasma power is enhanced. This consistency in the CO and $\rm H_2$ trend highlights the crucial role of the catalyst towards selectivity or global reaction pathway.

The $\rm H_2/CO$ ratio presented in Fig. 8(c) again verifies NO catalyst superiority in $\rm H_2$ production compared with NC catalyst. Carbon balance in the same plot shows higher coke formation (19.98 %) for the NO catalyst, likely due to increased conversions leading to possibilities of enhanced carbon formation reactions such as CH₄ cracking, steam generation, Boudouard, and CO reduction mentioned in Table S2. Determining the dominant carbon-forming reaction is challenging due to the complex interplay between plasma and thermal mechanisms. Regarding $\rm C_2H_6$ production, the NC catalyst exhibits relatively higher performance than the NO catalyst at lower plasma power, indicating the preference for $\rm C_2H_6$ generation. The $\rm C_2H_6$ production declines with increasing plasma power, consistent with the thermal effect observed.

In this section observation, the temperature stayed constant for both catalysts, ensuring EE could effectively compare catalyst efficiency. The EE shows an exciting trend with increasing plasma power for both catalysts, as shown in Fig. 8(d). The EE decreases with plasma power for the NC catalyst, having a maximum value of 4.9 mmol/kJ at the lowest plasma power (SIE 1.42 kJ/L). On the other hand, the NO catalyst follows a similar decreasing trend until the SIE of 3.95 kJ/L, after which it increases and reaches 4.7 mmol/kJ, which is quite interesting. The effect should be increased conversion at higher plasma power, which could be attributed to better plasma-catalyst interaction, leading to changes in the surface properties and the creation of additional active sites at higher plasma power for the NO catalyst.

3.5. Spent catalyst characterization

After undergoing multiple experimental cycles and an 11 h continuous plasma DRM experiment at 350 $^{\circ}$ C with approximately 12 W plasma power, the spent catalysts were subjected to various characterization techniques for further analysis. The XRD patterns of both spent 10 wt% Ni-CeO₂ catalysts and quartz wool (catalyst bed/holding material) are shown in Fig. 9(a) and 9(b). Both spent catalysts display CeO₂ and NiO peaks in their XRD pattern, indicating no structural alterations

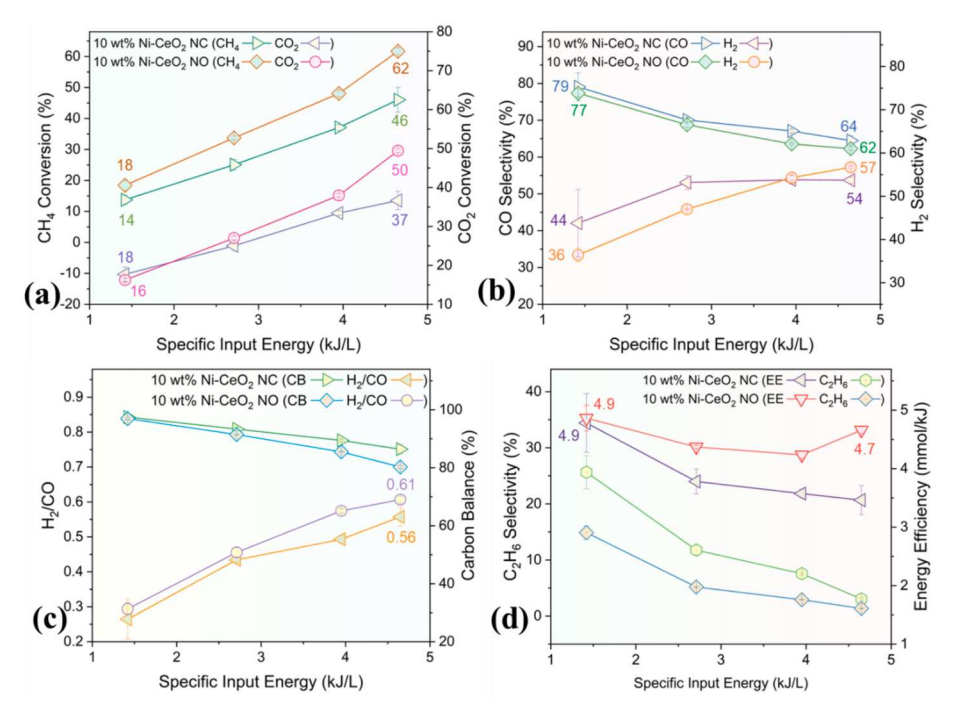


Fig. 8. Plasma power effect on 10 wt% Ni-CeO₂ catalysts' performance; (a) CH₄ and CO₂ conversion (b) CO and H₂ selectivity (c) H₂/CO ratio and carbon balance (d) C₂H₆ selectivity and energy efficiency. [Flow (sccm): CH₄/CO₂ = 100/250 = 0.4, Power: 8.3 to 27.1 W, Temperature: 350 °C].

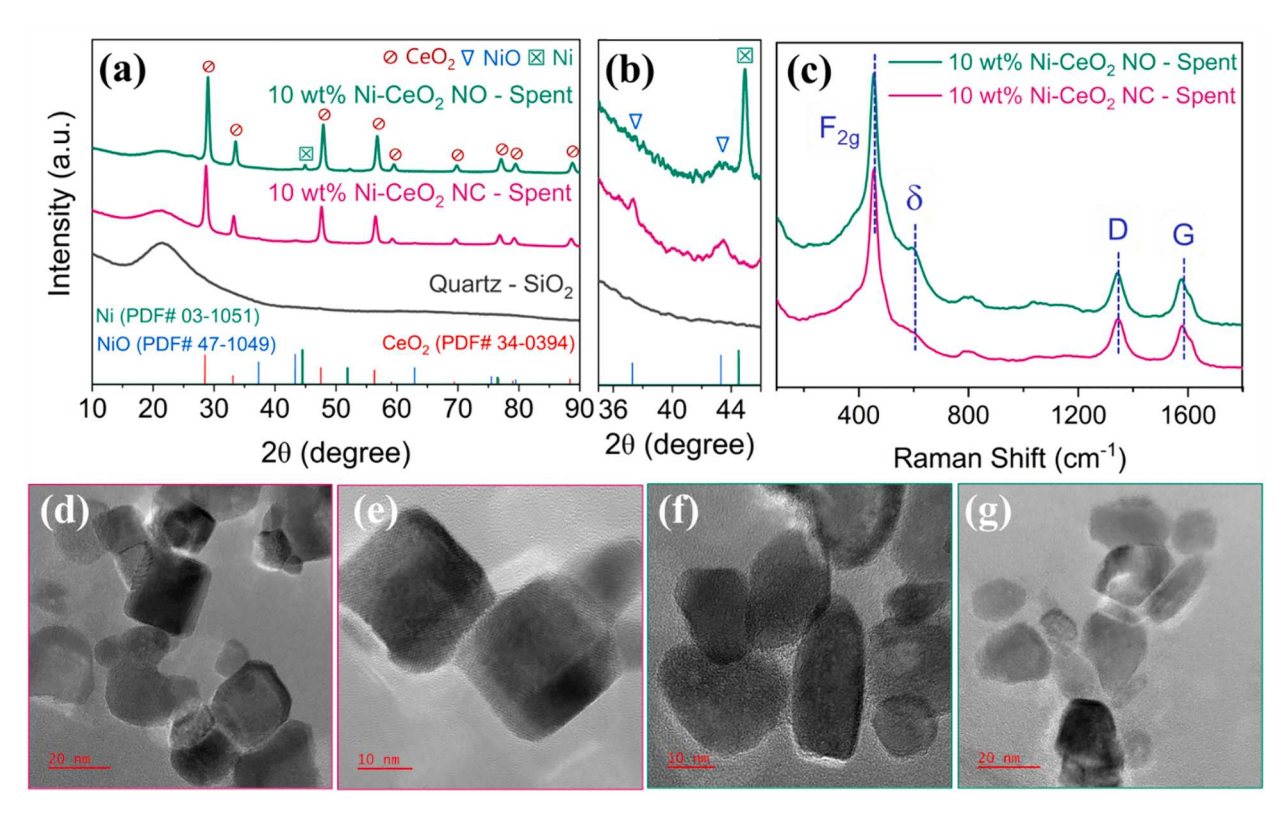


Fig. 9. (a) XRD pattern of spent 10 wt% Ni-CeO₂ catalysts and quartz wool (catalyst bed) (b) magnified XRD pattern (c) Raman spectra of spent 10 wt% Ni-CeO₂ catalysts, TEM and HRTEM images of spent (d, e) 10 wt% Ni-CeO₂ NC (f, g) 10 wt% Ni-CeO₂ NO catalyst.

after multiple experiments. Interestingly, the NO spent catalyst shows (111), (200), and (220) planes around 44.7°, 52.0°, and 76.6°, corresponding to the cubic phases of metallic Ni (PDF# 03–1051). The presence of metallic Ni suggests the reduction of the NiO phase, possibly due to the reaction with the DRM product $\rm H_2$. The amorphous peaks

around 20° observed in both catalysts are attributed to the quartz wool, which is also present in the fresh quartz wool (SiO₂) XRD pattern shown in Fig. 9(a).

The crystallite sizes of the fresh and spent 10 wt% Ni-CeO $_2$ catalysts are presented in Table 4. An intriguing observation is that after the

Table 4
Crystallite size and relative defect concentration for fresh and spent catalysts.

	Crystallite Size (nm) ^a			F _{2g} Peak	I _δ /	I _D /
Sample	(200)	(220)	(111)	Location (cm ⁻¹)	I_{F2g}^{b}	I_G^c
10 wt% Ni-CeO ₂ NC	14.69	15.94	14.28	447	0.20	
10 wt% Ni- CeO ₂ NC – Spent	14.87	17.69	16.24	454	0.23	0.85
10 wt% Ni- CeO ₂ NO	15.22	16.30	16.24	445	0.19	
$10 \text{ wt}\% \text{ Ni-} $ $\text{CeO}_2 \text{ NO} - $ Spent	13.30	14.02	14.08	456	0.34	0.85

^a Calculated using Scherrer equation; ^b Calculated from Raman analysis considering δ and $F_{2\alpha}$ peak; ^c considering D and G peak.

plasma-assisted DRM reactions, the NC spent catalysts show larger crystallite sizes than the fresh catalysts and the NO catalyst exhibits the opposite effect. This suggests distinct plasma interaction with each catalyst and potential modifications in the catalyst during the plasma DRM reaction, as typically observed for plasma-treated catalysts [64]. The reason could be the prolonged plasma environmental electron impact effect that deforms/strains CeO₂ crystal and affects crystallite size. However, the synthesized catalyst shapes remain unchanged after several plasma DRM cycle experiments, as confirmed by HRTEM analysis in Fig. 9(d-g).

The Raman spectra for both spent 10 wt% Ni-CeO $_2$ catalysts are shown in Fig. 9(c), and the corresponding defect concentration and F_{2g} peak location are presented in Table 4. The F_{2g} peak of the spent

catalysts shifted towards higher wavenumber values compared to the fresh catalysts, indicating variation of interatomic force due to bond length [43]. A probable reason for this shift may be attributed to the reduction of NiO species or the re-oxidation of NiO_x-CeO₂ solid solutions during the DRM process. The defects' concentration listed in Table 4 clearly indicates that subjecting the catalysts to plasma DRM reaction leads to increased defects in the lattice compared to fresh catalysts. Another study also observed increasing defect phenomenon in toluene oxidation reactions [65]. Comparing both spent catalysts, the NO catalyst has the highest defect concentration. Additionally, in both spent catalysts' spectra, the presence of two peaks, namely the G-band associated with sp² hybridized carbon atoms in graphitic structures and the D-band associated with sp² carbon atoms in disordered or defective structures, confirms the presence of both amorphous and graphite carbon in the catalyst [66]. The degree of graphite in the deposited carbon is calculated based on the intensity ratio of the D and G bands, providing insights into the carbon structure stability with the catalysts [67]. From Table 4 data, both spent catalysts have a similar D/G intensity ratio, indicating identical caron structure stability. In this study, the predominant form of carbon is observed as amorphous and gasified during the plasma regeneration cycle, as evidenced in Fig. S3. The morphology of the deposited carbon is in nanotube form, which is analyzed through SEM in Fig. S8.

The elemental distribution was analyzed for spent 10 wt% Ni-CeO $_2$ catalysts using EDS, as shown in Fig. 10. The SEM images in Fig. 10(a) and 10(g) represent agglomeration; the NC catalyst exhibits more agglomeration, while the NO catalyst shows less, which is the opposite of what is observed with each type of fresh catalyst. As in Fig. 10(e), the NC spent catalyst has a roughly uniform distribution of Ni in all areas, with some areas becoming agglomerated. However, in the case of the

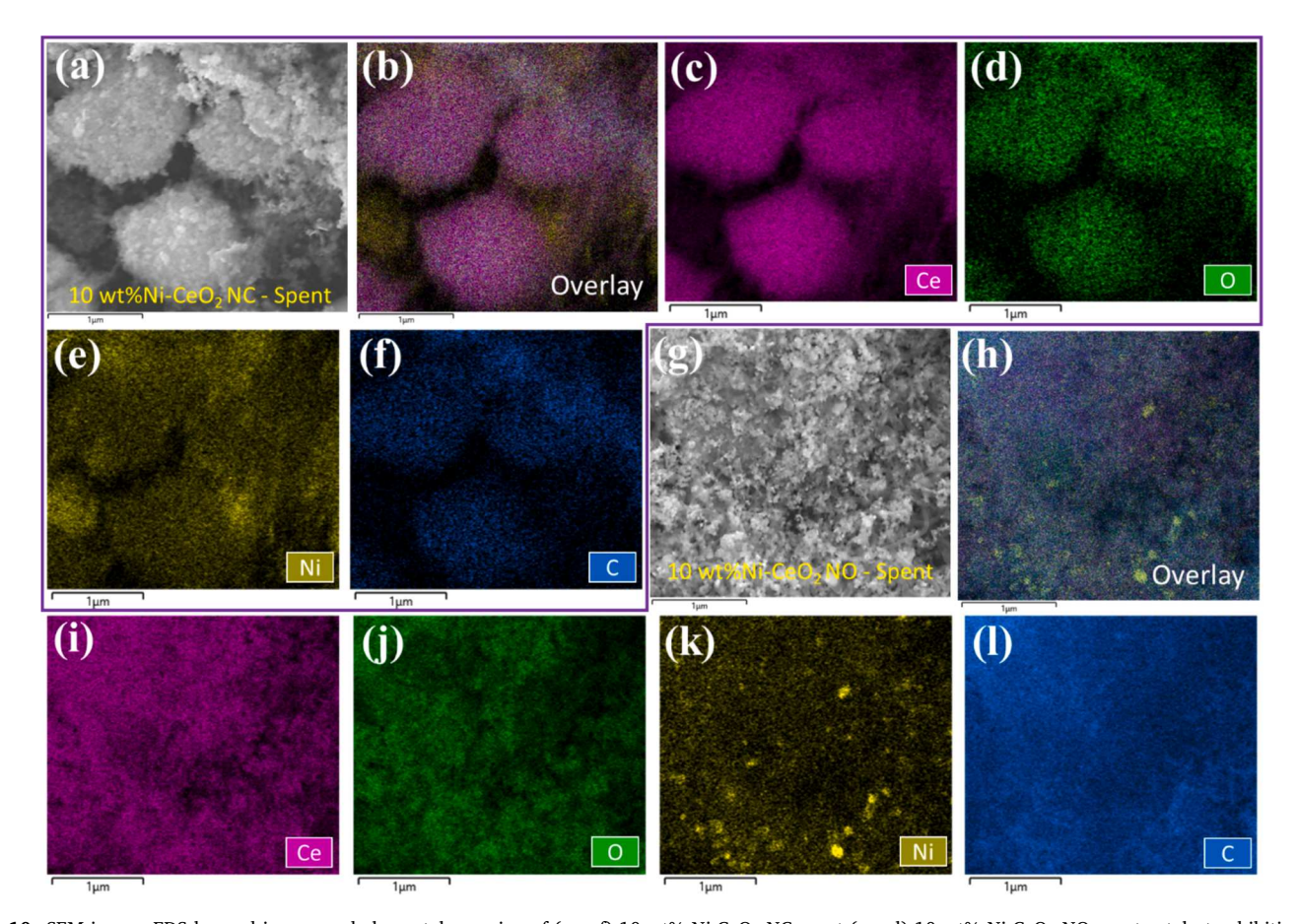


Fig. 10. SEM image, EDS layered image, and elemental mapping of (a - f) 10 wt% Ni-CeO₂ NC spent (g - l) 10 wt% Ni-CeO₂ NO spent catalyst exhibiting the elemental distribution.

NO spent catalyst, several concentrated Ni particles are observed on the CeO_2 surfaces, as shown in Fig. $10(\mathbf{k})$. This phase separation and concentrated Ni particles may be attributed to extended exposure to the plasma DRM environment. The presence of metallic Ni particles was also confirmed through XRD analysis, as shown in Fig. $9(\mathbf{a})$. There is convincingly uniform carbon deposition varying in concentration with Ce-O element, as shown in Fig. $10(\mathbf{f})$ for NC spent catalyst. However, the NO spent catalyst shows more localized concentrations of carbon, which could be due to differences in carbon deposition, as shown in Fig. $10(\mathbf{k})$. Additionally, carbon nanotubes were observed on both catalyst surfaces, as depicted in Fig. S8. The results suggest that a cyclical DRM and CO_2 regeneration approach is more suitable rather than a continuous DRM reaction.

3.6. Reaction insights of this study considering prior research

The distinct catalytic performances of both 10~wt% Ni-CeO $_2$ catalysts are attributed to their unique characteristics ultimately linked to morphology. Existing literature has proposed various reaction analyses based on experimental and simulation findings. A simplified analysis for the tested catalysts in this plasma-assisted DRM process is presented in Fig. 11.

In this analysis, CH₄ typically adsorbs on NiO_x active sites on the catalyst surface (CH_{4(g)} + NiO_x \rightarrow CH₄ (ads)), while CO₂ interacts with CeO₂ oxygen vacancies (CO_{2(g)} + CeO₂ \rightarrow CO₂ (ads)). In the presence of plasma, CH₄ is also adsorbed at Ni-CeO₂ interfaces as analyzed in literature [68], leading to increased CH₄ conversion in the plasma environment for both catalysts. The adsorbed CO₂ dissociates on CeO₂ surfaces, yielding CO (CO₂ (ads) + O_V \rightarrow CO(g) + O') and filling oxygen vacancy sites [69]. The involvement of metastable oxygen (O') also aligns with the experiment result where O' from CO₂ dissociation on the CeO₂ surface and/or lattice oxygen of CeO₂ produces CO by reacting with CH₄ (CH₄ (ads) + O_L or (O') \rightarrow CH₃*+ H₂O \rightarrow CO(g) + O²_(ads)) [70]. Both CH₄ and CO₂ undergo dissociation through plasma electron impact reactions, participate in the previously mentioned reactions, and expedite the reaction process.

In this study, the 10 wt% Ni-CeO $_2$ NO catalyst has more lattice defects, oxygen vacancy concentration, and basic sites than the NC catalyst. These characteristics make the NO catalyst different, which leads to higher conversions during plasma DRM. The difference in characteristics are intricately related to catalyst morphology.

4. Conclusions

This manuscript comprehensively studies 10 wt% Ni-CeO2 NC and 10 wt% Ni-CeO2 NO shaped catalysts in plasma-assisted DRM environment to investigate morphological effect on performance. Various characterization techniques uncovered distinct structural and surface properties. Structural analyses revealed a mixture of (100) and (111) planes present in both catalysts but predominant planes of (100) for 10 wt% Ni-CeO2 NC shape and (111) for 10 wt% Ni-CeO2 NO shape catalyst. These surface-exposed plane variations affect NiOx interaction with CeO₂, oxygen vacancy concentration, and other properties. The 10 wt% Ni-CeO2 NO-shaped catalyst exhibited increased oxygen vacancy concentration, additional lattice defects, and moderate basic sites compared to the 10 wt% Ni-CeO₂ NC-shaped catalyst. Catalytic performance was assessed under changing temperature and plasma power. The results revealed both catalysts' increased CH₄ and CO₂ conversions with rising temperature or plasma power, with better performance observed for 10 wt% Ni-CeO₂ NO catalyst. The CO selectivity decreased, while H2 selectivity increased with temperature or plasma power enhancements for both catalysts. This consistent trend confirms catalysts' dominance in controlling selectivity. Morphological analysis on spent catalysts confirmed shape preservation, enrichment of surface defects, and NiO phase separation, revealing amorphous carbon in nanotube forms. This deposited carbon can be easily gasified, and catalyst-active

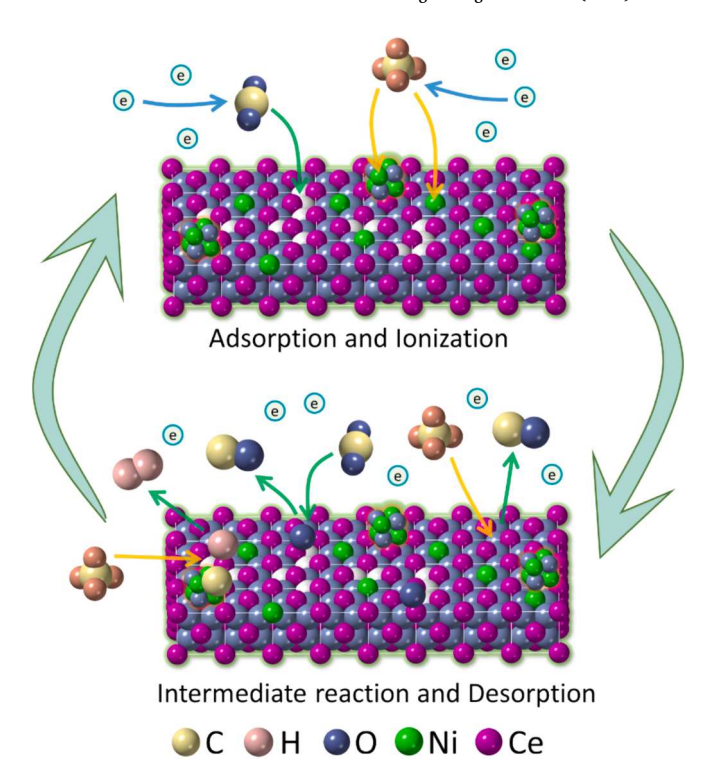


Fig. 11. Reaction analysis for shape-controlled plasma-assisted DRM.

sites can be regenerated through CO₂ oxidation in the plasma environment. Overall, this study demonstrates the potential of the catalyst shape effect for improving performance in plasma-assisted DRM processes.

CRediT authorship contribution statement

Md Monir Hossain: Writing – review & editing, Writing – original draft, Methodology, Investigation, Formal analysis. Md Robayet Ahasan: Formal analysis. Ruigang Wang: Writing – review & editing, Writing – original draft, Visualization, Validation, Supervision, Resources, Project administration, Methodology, Investigation, Funding acquisition, Formal analysis, Data curation, Conceptualization.

Declaration of competing interest

The authors declare that they have no known competing financial interests or personal relationships that could have appeared to influence the work reported in this paper.

Data availability

No data was used for the research described in the article.

Acknowledgments

This work is supported by the National Science Foundation (1856729, 2044733, and 2427213) and the use of SEM, TEM facilities at the Alabama Analytical Research Center (AARC) at The University of Alabama is gratefully acknowledged.

Appendix A. Supplementary data

Supplementary data to this article can be found online at https://doi.org/10.1016/j.cej.2024.154193.

References

- Overview | Energy economics | Home, (n.d.). https://www.bp.com/en/global/ corporate/energy-economics/energy-outlook/overview.html (accessed April 23, 2024).
- [2] EDGAR The Emissions Database for Global Atmospheric Research, (n.d.). https://edgar.jrc.ec.europa.eu/report_2023?vis=co2tot#emissions_table (accessed April 23, 2024).
- [3] V. Havran, M.P. Duduković, C.S. Lo, Conversion of methane and carbon dioxide to higher value products, Ind. Eng. Chem. Res. 50 (2011) 7089–7100.
- [4] A. Abdulrasheed, A.A. Jalil, Y. Gambo, M. Ibrahim, H.U. Hambali, M.Y. Shahul Hamid, A review on catalyst development for dry reforming of methane to syngas: Recent advances, Renew. Sustain. Energy Rev. 108 (2019) 175–193.
- [5] A.G.S. Hussien, K. Polychronopoulou, A Review on the Different Aspects and Challenges of the Dry Reforming of Methane (DRM) Reaction, Nanomaterials (basel), 12 (2022) 3400.
- [6] E. le Saché, T.R. Reina, Analysis of Dry Reforming as direct route for gas phase CO2 conversion, The past, the Present and Future of Catalytic DRM Technologies, Prog Energy Combust Sci. 89 (2022) 100970.
- [7] L. Li, S. Wang, L. Xiong, B. Wang, G. Yang, S. Yang, Surface-engineered mesoporous Pt nanodendrites with Ni dopant for highly enhanced catalytic performance in hydrogen evolution reaction, J Mater Chem A Mater. 7 (2019) 12800–12807.
- [8] F. Polo-Garzon, Z. Bao, X. Zhang, W. Huang, Z. Wu, Surface Reconstructions of Metal Oxides and the Consequences on Catalytic Chemistry, ACS Catal. 9 (2019) 5692–5707.
- [9] Y. Wang, N. Wang, J. Harding, G. Chen, X. Tu, Plasma technology for syngas production, Advances in Synthesis Gas: Methods, Technologies and Applications. (2023) 327–359.
- [10] X. Li, D. Li, H. Tian, L. Zeng, Z.J. Zhao, J. Gong, Dry reforming of methane over Ni/ La2O3 nanorod catalysts with stabilized Ni nanoparticles, Appl Catal B 202 (2017) 683–694.
- [11] J.J. González, J.F. Da Costa-Serra, A. Chica, Biogas dry reforming over Ni–Ce catalyst supported on nanofibered alumina, Int. J. Hydrogen Energy 45 (2020) 20568–20581.
- [12] D. Shen, M. Huo, L. Li, S. Lyu, J. Wang, X. Wang, Y. Zhang, J. Li, Effects of alumina morphology on dry reforming of methane over Ni/Al2O3 catalysts, Catal, Sci. Technol. 10 (2020) 510–516.
- [13] R. Tan, P. Wang, L. Guo, Z. Chen, R. Lin, X. Mou, Y. Ding, Nickel-Catalyzed Dry Reforming of Methane via Modulating the Zirconia Shapes, ChemCatChem 15 (2023) e202300136.
- [14] A.H. Khoja, M. Tahir, N.A.S. Amin, Recent developments in non-thermal catalytic DBD plasma reactor for dry reforming of methane, Energy Convers Manag. 183 (2019) 529–560.
- [15] D. Wang, P. Littlewood, T.J. Marks, P.C. Stair, E. Weitz, Coking Can Enhance Product Yields in the Dry Reforming of Methane, ACS Catal. 12 (2022) 8352–8362.
- [16] B. Wang, B. Chen, Y. Sun, H. Xiao, X. Xu, M. Fu, J. Wu, L. Chen, D. Ye, Effects of dielectric barrier discharge plasma on the catalytic activity of Pt/CeO2 catalysts, Appl Catal B 238 (2018) 328–338.
- [17] Z. Wang, Y. Zhang, E.C. Neyts, X. Cao, X. Zhang, B.W.L. Jang, C.J. Liu, Catalyst Preparation with Plasmas: How Does It Work? ACS Catal. 8 (2018) 2093–2110.
- [18] H. Taghvaei, M. Heravi, M.R. Rahimpour, Synthesis of supported nanocatalysts via novel non-thermal plasma methods and its application in catalytic processes, Plasma Processes Polym. 14 (2017) 1600204.
- [19] L. Pastor-Pérez, V. Belda-Alcázar, C. Marini, M.M. Pastor-Blas, A. Sepúlveda-Escribano, E.V. Ramos-Fernandez, Effect of cold Ar plasma treatment on the catalytic performance of Pt/CeO2 in water-gas shift reaction (WGS), Appl Catal B 225 (2018) 121–127.
- [20] P. Pérez-Bailac, P.G. Lustemberg, M.V. Ganduglia-Pirovano, Facet-dependent stability of near-surface oxygen vacancies and excess charge localization at CeO2 surfaces, J. Phys. Condens. Matter 33 (2021) 504003.
- [21] Y. Wang, R. Wang, Effects of chemical etching and reduction activation of CeO2 nanorods supported ruthenium catalysts on CO oxidation, J. Colloid Interface Sci. 613 (2022) 836–846.
- [22] Y. Wang, Z. Liu, R. Wang, NaBH4 Surface Modification on CeO2 Nanorods Supported Transition-Metal Catalysts for Low Temperature CO Oxidation, ChemCatChem 12 (2020) 4304–4316.
- [23] Z. Wei, R. Wang, Chemically etched CeO2-x nanorods with abundant surface defects as effective cathode additive for trapping lithium polysulfides in Li-S batteries, J. Colloid Interface Sci. 615 (2022) 527–542.
- [24] S. Azam, Z. Wei, R. Wang, Cerium oxide nanorods anchored on carbon nanofibers derived from cellulose paper as effective interlayer for lithium sulfur battery, J. Colloid Interface Sci. 615 (2022) 417–431.
- [25] S. Azam, Z. Wei, R. Wang, Adsorption-catalysis design with cerium oxide nanorods supported nickel-cobalt-oxide with multifunctional reaction interfaces for anchoring polysulfides and accelerating redox reactions in lithium sulfur battery, J. Colloid Interface Sci. 635 (2023) 466–480.
- [26] M.R. Ahasan, M.M. Hossain, X. Ding, R. Wang, Non-equilibrium plasma-assisted dry reforming of methane over shape-controlled CeO2 supported ruthenium catalysts, J Mater Chem A Mater. 11 (2023) 10993–11009.
- [27] M.R. Ahasan, Y. Wang, R. Wang, In situ DRIFTS and CO-TPD studies of CeO2 and SiO2 supported CuOx catalysts for CO oxidation, Mol. Catal. 518 (2022) 112085.
- [28] Y. Wang, Z. Liu, M.P. Confer, J. Li, R. Wang, In-situ DRIFTS study of chemically etched GeO2 nanorods supported transition metal oxide catalysts, Mol. Catal. 509 (2021) 111629.

- [29] R. V Ranganathan, M. Monir Hossain, S. Talukdar, R. Ahasan, R. Wang, M. Uddi, Tunable Quantum Cascade Laser Absorption Spectroscopy for Plasma Assisted Oxidative Coupling of Methane to C 2 Based Products, (2021) 1–1.
- [30] A. Trovarelli, J. Llorca, Ceria Catalysts at Nanoscale: How Do Crystal Shapes Shape Catalysis? ACS Catal. 7 (2017) 4716–4735.
- [31] J. Li, Z. Liu, D.A. Cullen, W. Hu, J. Huang, L. Yao, Z. Peng, P. Liao, R. Wang, Distribution and Valence State of Ru Species on CeO2 Supports: Support Shape Effect and Its Influence on CO Oxidation, ACS Catal. 9 (2019) 11088–11103.
- [32] R. Wang, R. Dangerfield, Seed-mediated synthesis of shape-controlled CeO2 nanocrystals, RSC Adv. 4 (2013) 3615–3620.
- [33] M.M. Hossain, M.R. Ahasan, X. Ding, R. Wang, Coke formation pathway under various reaction conditions during the production of syngas in a dielectric barrier discharge plasma environment using CeO2 nanorods supported Ni catalysts, Chem. Eng. J. 479 (2024) 147459.
- [34] M.R. Ahasan, M.M. Hossain, Z. Barlow, X. Ding, R. Wang, Low-temperature plasma-assisted catalytic dry reforming of methane over CeO2 nanorod-supported NiO catalysts in a dielectric barrier discharge reactor, ACS Appl. Mater. Interfaces 15 (2023) 44984–44995.
- [35] M. Hotub, On the measurement of plasma power in atmospheric pressure DBD plasma reactors, Int. J. Appl. Electromagn. Mech. 39 (2012) 81–87.
- [36] Y. Xie, J. Chen, X. Wu, J. Wen, R. Zhao, Z. Li, G. Tian, Q. Zhang, P. Ning, J. Hao, Frustrated Lewis pairs boosting low-temperature CO 2 methanation performance over Ni/CeO 2 nanocatalysts, ACS Catal. 12 (2022) 10587–10602.
- [37] Y. Bian, C. Xu, X. Wen, L. Xu, Y. Cui, S. Wang, C.E. Wu, J. Qiu, G. Cheng, M. Chen, CO2 methanation over the Ni-based catalysts supported on nano-CeO2 with varied morphologies, Fuel 331 (2023) 125755.
- [38] M. Shaw, D. Samanta, M.A.S. Shaik, R. Basu, D. Das, A. Pathak, Ethanol gas sensors using semi-Hedgehog-like CuO nanostructures: studying the role of oxygen vacancies, unsaturated Cu-sites, and hole accumulation layer, ACS Appl Nano Mater. 6 (2023) 21839–21852.
- [39] S. Shah, M. Xu, X. Pan, K.L. Gilliard-Abdulaziz, Exsolution of Embedded Ni-Fe-Co Nanoparticles: implications for Dry Reforming of Methane, ACS Appl Nano Mater. 4 (2021) 8626–8636.
- [40] T. Li, H. Wang, Y. Yang, H. Xiang, Y. Li, Study on an iron-nickel bimetallic Fischer-Tropsch synthesis catalyst, Fuel Process. Technol. 118 (2014) 117–124.
- [41] R. Khatun, R.S. Pal, M.A. Shoeb, D. Khurana, S. Singhl, N. Siddiqui, M.K. Poddar, T. S. Khan, R. Bal, Generation of active oxygen species by CO2 dissociation over defect-rich Ni-Pt/CeO2 catalyst for boosting methane activation in low-temperature dry reforming: Experimental and theoretical study, Appl. Catal. B 340 (2024) 123243.
- [42] D. Shen, Z. Li, J. Shan, G. Yu, X. Wang, Y. Zhang, C. Liu, S. Lyu, J. Li, L. Li, Synergistic Pt-CeO2 interface boosting low temperature dry reforming of methane, Appl. Catal. B 318 (2022) 121809.
- [43] B. Liu, C. Li, G. Zhang, X. Yao, S.S.C. Chuang, Z. Li, Oxygen Vacancy Promoting Dimethyl Carbonate Synthesis from CO2 and Methanol over Zr-Doped CeO2 Nanorods, ACS Catal. 8 (2018) 10446–10456.
- [44] M. Romeo, K. Bak, J. El Fallah, F. Le Normand, L. Hilaire, XPS Study of the reduction of cerium dioxide, Surface and Interface, Analysis 20 (1993) 508–512.
- [45] J. Niu, C. Zhang, H. Liu, Y. Jin, R. Zhang, Enhanced performance of oxygen vacancies on CO2 adsorption and activation over different phases of ZrO2, Front. Energy 17 (2023) 545–554.
- [46] P.G. Lustemberg, Z. Mao, A. Salcedo, B. Irigoyen, M.V. Ganduglia-Pirovano, C. T. Campbell, Nature of the Active Sites on Ni/CeO2Catalysts for Methane Conversions, ACS Catal. 11 (2021) 10604–10613.
- [47] H. Prats, R.A. Gutiérrez, J.J. Pinero, F. Vines, S.T. Bromley, P.J. Ramírez, J. A. Rodriguez, F. Illas, Room Temperature Methane Capture and Activation by Ni Clusters Supported on TiC(001): Effects of Metal-Carbide Interactions on the Cleavage of the C-H Bond, J. Am. Chem. Soc. 141 (2019) 5303–5313.
- [48] A.P. Grosvenor, M.C. Biesinger, R.S.C. Smart, N.S. McIntyre, New interpretations of XPS spectra of nickel metal and oxides, Surf. Sci. 600 (2006) 1771–1779.
- [49] S. López-Rodríguez, A. Davó-Quiñonero, E. Bailón-García, D. Lozano-Castelló, I. J. Villar-García, V.P. Dieste, J.A.O. Calvo, J.R.G. Velasco, A. Bueno-López, Monitoring by in situ NAP-XPS of active sites for CO2 methanation on a Ni/CeO2 catalyst, J. CO2 Util. 60 (2022) 101980.
- [50] S. Gao, Y. Li, W. Guo, X. Ding, L. Zheng, L. Wu, H. Yan, Y. Wang, Morphology effect of ceria support with hierarchical structure on the catalytic performance for nickelbased catalysts in dry reforming of methane, Mol. Catal. 533 (2022) 112766.
- [51] A.L.A. Marinho, F.S. Toniolo, F.B. Noronha, F. Epron, D. Duprez, N. Bion, Highly active and stable Ni dispersed on mesoporous CeO2-Al2O3 catalysts for production of syngas by dry reforming of methane, Appl Catal B 281 (2021) 119459.
- [52] G.I. Siakavelas, N.D. Charisiou, S. AlKhoori, A.A. AlKhoori, V. Sebastian, S. J. Hinder, M.A. Baker, I.V. Yentekakis, K. Polychronopoulou, M.A. Goula, Highly selective and stable nickel catalysts supported on ceria promoted with Sm2O3, Pr2O3 and MgO for the CO2 methanation reaction, Appl Catal B 282 (2021) 119562.
- [53] A. Cárdenas-Arenas, A. Quindimil, A. Davó-Quiñonero, E. Bailón-García, D. Lozano-Castelló, U. De-La-Torre, B. Pereda-Ayo, J.A. González-Marcos, J. R. González-Velasco, A. Bueno-López, Isotopic and in situ DRIFTS study of the CO2 methanation mechanism using Ni/CeO2 and Ni/Al2O3 catalysts, Appl Catal B 265 (2020) 118538.
- [54] A. Cárdenas-Arenas, A. Quindimil, A. Davó-Quiñonero, E. Bailón-García, D. Lozano-Castelló, U. De-La-Torre, B. Pereda-Ayo, J.A. González-Marcos, J. R. González-Velasco, A. Bueno-López, Design of active sites in Ni/CeO2 catalysts for the methanation of CO2: tailoring the Ni-CeO2 contact, Appl. Mater. Today 19 (2020) 100591.

- [55] E. Yang, E. Nam, Y. Jo, K. An, Coke resistant NiCo/CeO2 catalysts for dry reforming of methane derived from core@shell Ni@Co nanoparticles, Appl Catal B 339 (2023) 123152.
- [56] S.N.A. Rosli, S.Z. Abidin, O.U. Osazuwa, X. Fan, Y. Jiao, The effect of oxygen mobility/vacancy on carbon gasification in nano catalytic dry reforming of methane: A review, J. CO2 Util. 63 (2022) 102109.
- [57] X. Tu, H.J. Gallon, M.V. Twigg, P.A. Gorry, J.C. Whitehead, Dry reforming of methane over a Ni/Al2O3 catalyst in a coaxial dielectric barrier discharge reactor, J. Phys. D Appl. Phys. 44 (2011) 274007.
- [58] Y.R. Luo, Comprehensive handbook of chemical bond energies, Comprehensive Handbook of Chemical Bond Energies. (2007) 1–1656.
- [59] R.V. Ranganathan, B. Jony, S.M. Fondriest, Z. Liu, R. Wang, M. Uddi, Plasmacatalysis chemical looping CH4 reforming with water splitting using ceria supported Ni based La-perovskite nano-catalyst, J. CO2 Util. 32 (2019) 11–20.
- [60] H.J. Gallon, J. Whitehead, Dry Reforming of Methane Using Non-Thermal Plasma-Catalysis, 2010. https://www.proquest.com/dissertations-theses/dry-reforming-methane-using-non-thermal-plasma/docview/2055188831/se-2? accountid=14472.
- [61] Y. Diao, X. Zhang, Y. Liu, B. Chen, G. Wu, C. Shi, Plasma-assisted dry reforming of methane over Mo2C-Ni/Al2O3 catalysts: Effects of β-Mo2C promoter, Appl Catal B 301 (2022) 120779.
- [62] R.V. Ranganathan, Z. Liu, H. Menon, S. Talukdar, R. Wang, M. Uddi, Nanoshaped GeO 2 and SiO 2 Supported Ru Catalyst for Plasma Catalysis Chemical Looping Reactions, Int. J. Energy Eng. 2020 (2020) 67–79.

- [63] M.I. Malik, I.E. Achouri, N. Abatzoglou, F. Gitzhofer, Intensified performance of methane dry reforming based on non-thermal plasma technology: Recent progress and key challenges, Fuel Process. Technol. 245 (2023) 107748.
- [64] X. Zhu, P. Huo, Y. Ping Zhang, D. Guo Cheng, C. Jun Liu, Structure and reactivity of plasma treated Ni/Al2O3 catalyst for CO2 reforming of methane, Appl. Catal. B 81 (2008) 132–140.
- [65] B. Wang, N. Wang, Y. Sun, H. Xiao, M. Fu, S. Li, H. Liang, Z. Qiao, D. Ye, Dielectric barrier discharge plasma modified Pt/CeO2 catalysts for toluene oxidation: Effect of discharge time, Appl. Surf. Sci. 614 (2023) 156162.
- [66] A. Braga, M. Armengol-Profitós, L. Pascua-Solé, X. Vendrell, L. Soler, I. Serrano, I. J. Villar-Garcia, V. Pérez-Dieste, N.J. Divins, J. Llorca, Bimetallic NiFe Nanoparticles Supported on CeO2 as Catalysts for Methane Steam Reforming, ACS Appl. Nano Mater. 6 (2023) 7173–7185.
- [67] J. Zheng, S. Impeng, J. Liu, J. Deng, D. Zhang, Mo promoting Ni-based catalysts confined by halloysite nanotubes for dry reforming of methane: Insight of coking and H2S poisoning resistance, Appl. Catal. B 342 (2024) 123369.
- [68] Z. Lian, S.O. Olanrele, C. Si, M. Yang, B. Li, Critical role of interfacial sites between nickel and CeO2 support in dry reforming of methane: revisit of reaction mechanism and origin of stability, J. Phys. Chem. C 124 (2020) 5118–5124.
- [69] P. Djinović, J. Zavašnik, J. Teržan, I. Jerman, Role of CO2 during oxidative dehydrogenation of propane over bulk and activated-carbon supported cerium and vanadium based catalysts, Catal. Lett. 151 (2021) 2816–2832.
- [70] S. Das, A. Jangam, S. Jayaprakash, S. Xi, K. Hidajat, K. Tomishige, S. Kawi, Role of lattice oxygen in methane activation on Ni-phyllosilicate@Ce1-xZrxO2 core-shell catalyst for methane dry reforming: Zr doping effect, mechanism, and kinetic study, Appl. Catal. B 290 (2021) 119998.